

A geometry-dependent surface Lambertian-equivalent reflectivity product at 466 nm for UV/Vis retrievals: Part I. Evaluation over land surfaces using measurements from OMI

Wenhan Qin¹, Zachary Fasnacht¹, David Haffner¹, Alexander Vasilkov¹, Joanna Joiner², Nickolay Krotkov², Brad Fisher¹, and Robert Spurr³

¹Science Systems and Applications Inc., Lanham, MD, USA

²NASA Goddard Space Flight Center, Greenbelt, MD, USA

³Rt Solutions Inc., Cambridge, MA, USA

Correspondence to: W. Qin (wenhan.qin@ssaihq.com)

Abstract. The anisotropy of the Earth’s surface reflection has implications for satellite-based retrieval algorithms that utilize climatological surface reflectivity databases that do not depend upon the observation geometry. This is the case for most of the current ultraviolet and visible (UV/Vis) cloud, aerosol, and trace-gas algorithms. The illumination-observation dependence of surface reflection is described by the bidirectional reflectance distribution function (BRDF). To account for the BRDF effect, we use the concept of geometry-dependent surface Lambertian-equivalent reflectivity (GLER), which is derived from the top-of-atmosphere (TOA) radiance computed with Rayleigh scattering and surface BRDF for the exact geometry of a satellite-based pixel. We present details on the implementation of land and water surface BRDF models. ~~—, and We~~ evaluate our GLER product over land surfaces using observed ~~and computed~~ sun-normalized radiances at 466 nm. The input surface BRDF parameters for computing TOA radiance are derived from MODerate-resolution Imaging Spectroradiometer (MODIS) satellite observations. The observed TOA radiance for comparison is from the Ozone Monitoring Instrument (OMI). The comparison shows good agreement between observed and calculated OMI ~~radiances in reflectivity in 2006 in~~ typical geographical regions, with correlation coefficients greater than ~~0.9 for a majority of the selected regions in the year of 2006. 0.8 for some regions.~~ Seasonal variations of clear-sky OMI ~~radiances reflectivity~~ (i.e., with minimum clouds and aerosols) closely follow those computed using MODIS-derived GLER over land. GLER also captures the cross-track dependence of ~~OMI radiances, although the observations are OMI-derived LER, though the latter is~~ slightly higher than ~~those computed using GLER the former~~ presumably owing to residual cloud and aerosol (non-absorbing) contamination, particularly over dark surfaces (heavily vegetated regions such as mixed forest, croplands and grasslands).

Calibration differences between OMI and MODIS may also be responsible for some of this bias.

The standard OMI climatological surface reflectivity database predicts higher radiances than GLER and OMI observations with different seasonal ~~variations and cross-track dependence over most of the selected regions~~ variation over most regions and does not have any angular-dependent variation.

- 5 Overall, our evaluation demonstrates that the GLER product adequately accounts for surface BRDF effects while at the same time simplifies the surface BRDF implementation within the existing OMI retrieval infrastructure; use of our GLER product requires changes only to the input surface reflectivity database.

1 Introduction

10 It is well-known that reflection of the incident sunlight by the Earth's surface is generally anisotropic in the optical wavelength range (Rencz and Ryerson, 1999). Rough surfaces (vegetated landscapes, urban and built-up, bare soils, etc) usually exhibit marked backward scattering, whereas smooth surfaces (e.g., water, snow/ice) tend to have a strong forward scattering peak (specular reflection). Two well-known phenomena related to surface reflection anisotropy are the hot-spot effect over land
15 and the sunglint over ocean. The hot-spot effect occurs when the viewing direction coincides with the illumination direction, such that all shadows are invisible. This results in a reflectance peak in backward scattering directions (e.g., Qin et al., 1996). Sunglint, however, is a peak in forward scattering caused by Fresnel reflection over a smooth surface such as calm water, when sunlight reflects off the surface at the same angle that the surface is viewed (e.g., Kay et al., 2009).

20 The dependence of surface reflection on illumination and observation directions is mathematically described by the bidirectional reflectance distribution function (BRDF), an intrinsic property of the surface (Nicodemus, 1965; Martonchik et al., 2000; Schaepman-Strub et al., 2006). Since BRDF is defined in terms of differential solid angles, in theory it cannot be measured (Nicodemus, 1977). Therefore, another quantity which can be retrieved from remote sensing data, the bidirectional reflectance factor (BRF), has been widely used ever since. BRF is defined as the ratio of the reflected
25 radiance from the surface to that from a perfect Lambertian surface under the same geometry (illumination and observation) and ambient conditions. Since an ideal diffuse surface reflects the same radiance in all viewing directions, the BRDF for a Lambertian surface is $1/\pi$. Because of this, the BRF for any surface is equal to its BRDF times π . However, unlike the BRDF, BRF is a unitless
30 quantity.

The effect of surface anisotropy on satellite-observed radiances ~~propagates through the atmosphere and may in the visible is notable and neglect of it in retrievals can~~ produce complex errors. The influence of surface anisotropy on the top of the atmosphere (TOA) radiance increases with wavelength for a Rayleigh atmosphere (no aerosols or clouds) because atmospheric transmittance increases with
35 wavelength in the ultraviolet and visible (UV/Vis) spectral regions. ~~Under natural conditions for~~

~~Earth observing, the incident irradiance comprises~~ The radiation incident on the surface consists of
a direct component (non-scattered radiation) and a diffuse component scattered by the atmosphere
(gases, aerosols, and clouds)~~and by the surroundings of the observed surface (e.g., topography).~~

The magnitude and spectral distribution of the diffuse irradiance depends on atmospheric con-
5 ditions. Over a clear sky, the diffuse component originates from Rayleigh scattered sunlight that
follows a λ^{-4} dependence, where λ is wavelength. As a result, the surface anisotropy's impact
on TOA radiance is ~~very strong for~~ strong at visible or longer wavelengths ~~simply~~ because the at-
mosphere is ~~much more transparent at these wavelengths.~~ more transparent than in the UV where
Rayleigh scattered light is more prominent and therefore smooths and reduces the surface BRDF
10 effect at UV wavelengths. Obviously, the longer the wavelength, the stronger the effects, as shown
in Lorente et al. (2018) when comparing surface anisotropy effects in the near-infrared (NIR) with
that in the visible.

The surface reflectance anisotropy has implications for UV/Vis satellite retrievals of aerosols,
clouds, and trace gases such as nitrogen dioxide (NO₂). Currently, most satellite-based UV/Vis al-
15 gorithms (e.g., Krotkov et al., 2017) use surface reflectivity climatologies, typically gridded monthly
Lambertian-equivalent reflectivities (LERs) that have been derived from satellite ~~observations (e.g., Herman and Celarier, 1997; Koe-~~
for example, Herman and Celarier (1997) from the Total Ozone Mapping Spectrometer (TOMS) at
340 and 380 nm, Koelemeijer et al. (2001) from the Global Ozone Monitoring Experiment (GOME)
in 11 wavelengths between 335-772 nm, Kleipool et al. (2008) from OMI in 23 wavelengths at 328-499 nm,
20 and more recently Tilstra et al. (2017) from GOME-2 in 21 wavelengths between 335-772 nm as
well as from the Scanning Imaging Absorption Spectrometer for Atmospheric Chartography (SCIAMACHY)
in 29 wavelengths from 335-1670 nm. These climatologies are ~~typically constructed by statistically~~
analyzing constructed by computing statistical values representative of multiple years of observations
~~that have various Sun-viewing observations made with different sun and viewing geometries.~~ In or-
25 der to minimize cloud contamination, they may be based on a lower percentile (e.g., Herman and Celarier, 1997) and/or
the mode of the LER histogram depending on surface type (Kleipool et al., 2008) (e.g., Koelemeijer et al., 2001; Kleipool et al., 2008).
As pointed out recently by Lorente et al. (2018), such climatologies tend to pick up the lowest val-
ues among the measurements of a scene, typically corresponding with forward (backward) scattering
geometries over land (water).

30 An example of the impact of LER climatologies on cloud fraction retrievals is the presence of
considerable cross-track biases. This has been shown for satellite retrievals in the O₂-A band (Wang
et al., 2008) as well as for the 477 nm O₂-O₂ band (Veefkind et al., 2016). This happens because
the LER climatologies tend to underestimate the actual LER in the backward scattering directions
~~(usually the west side of the scan line) over land,~~ over land since the hot-spot phenomenon is not
35 represented properly and the retrieval compensates for this by overestimating cloud fractions in order
to match the observed TOA reflectance. Over ocean, such overestimation of cloud fraction would
occur in the forward scattering ~~directions (east side)~~ direction due to neglect of sun glint.

To account for surface anisotropy in existing cloud and trace gas algorithms that ~~make use of the~~ use LER, we implement the concept of geometry-dependent LER (GLER), which was introduced by Vasilkov et al. (2017). GLER is derived from simulated TOA radiance of a Rayleigh atmosphere over a non-Lambertian surface for the specific geometry of a satellite pixel. Here “geometry-dependent” is emphasized to distinguish the GLER product (which considers the angular dependence of surface reflection) from other LER-related products or climatologies that have no dependence on sun/satellite geometries. Our GLER approach does not require major changes to existing trace gas and cloud algorithms that rely on an estimate of LER (Vasilkov et al., 2017); the main revision to the algorithms requires replacement of the existing static LER climatologies with ~~GLERs~~ GLER calculated for specific fields-of-view (FOVs) and Sun-satellite geometries. ~~GLERs~~ GLER can be applied to any satellite retrieval algorithm that uses ~~LERs~~ LER.

The main goal of this paper is to evaluate our GLER product over land surfaces using visible measurements from the satellite-borne Ozone Monitoring Instrument (OMI). In the current version, the GLER is based on BRDF parameters derived from MODerate-resolution Imaging Spectroradiometer (MODIS) satellite observations over land; we plan to cover the ocean results in a separate paper. We also provide additional details on the GLER methodology, including the determination of the product components and key input model parameters. Specifically, ~~models used for surface BRDF~~ models and atmospheric radiative transfer (RT) calculations ~~for both atmosphere and surfaces as well as the MODIS BRDF product~~ are introduced in Section 2. We compare OMI-measured and simulated ~~TOA radiances and LERs~~ LER over typical geographical regions as a function of cross-track position, season, and year in Section 3. Discussion and conclusions are provided in the final two sections.

2 Data and Methods

In this section, we describe data sets and methodologies used to estimate each component of GLER. The implementation and validation process is summarized in Figure 1. ~~The~~ In the following, we first briefly introduce the surface BRDF models used for GLER computation.

2.1 Surface BRDF models

The kernel-driven BRDF model from the MODIS BRDF/Albedo algorithm (Lucht et al., 2000) is used in this study to describe land surface reflection anisotropy. This model is also known as the Ross-Thick/Li-Sparse Reciprocal (RTLS). RTLS consists of a linear combination of the weighted sum of an isotropic parameter and two kernels that characterize the scattering dependence on viewing and illumination geometry (Roujean et al., 1992). The Ross-Thick kernel is derived from radiative transfer models (Ross, 1981) for volume scattering within a dense vegetation canopy, and the Li-Sparse Reciprocal kernel is based on surface scattering and geometric shadow-casting with mutual shadowing

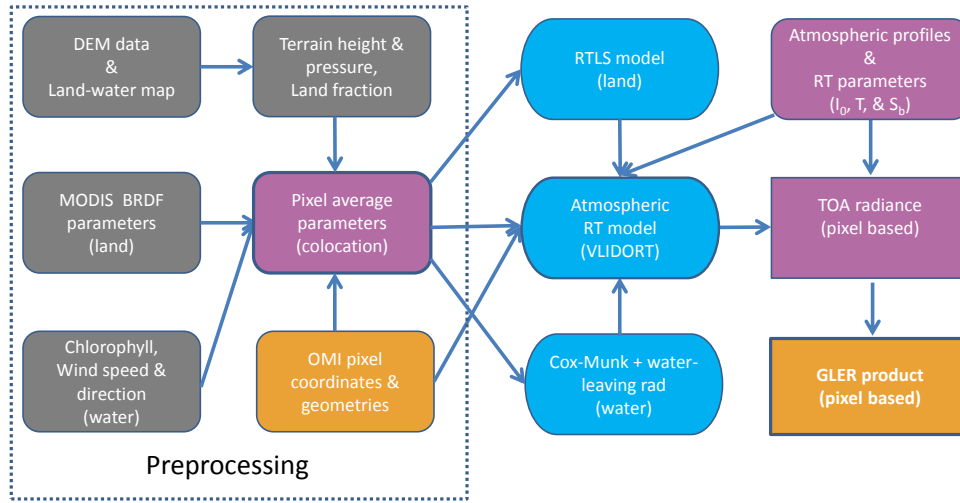


Fig. 1: Flowchart of the GLER processes. Different colors stand for different data types/sources: grey for ancillary data for both land and water, purple for preprocessed input parameters or atmospheric input parameters, gold for sensor-dependent pixel-related inputs/output, and finally, blue ovals for the physical models used. All input data are represented by the rounded rectangles and output product is shown in the box rectangle. DEM denotes digital elevation model. RTLS denotes the Ross-Thick/Li-Sparse Reciprocal functions (see Section 2.1 for details). Also see Eq. 2 for definitions of I_0 , T and S_b .

theory (Li and Strahler, 1992).

The mathematical expression for the kernel-driven RTLS to estimate surface BRDF is as follows:

$$\text{BRF}(\lambda, \theta, \theta_0, \phi) = f_{\text{iso}}(\lambda) + f_{\text{vol}}(\lambda)k_{\text{vol}}(\theta, \theta_0, \phi) + f_{\text{geo}}(\lambda)k_{\text{geo}}(\theta, \theta_0, \phi), \quad (1)$$

- 5 where θ is the viewing zenith angle (VZA), θ_0 the solar zenith angle (SZA), and ϕ the relative azimuth angle (RAA). k_{vol} and k_{geo} are the Ross-Thick and Li-Sparse Reciprocal kernels; f_{iso} , f_{vol} and f_{geo} are the kernel weights (also called kernel coefficients or BRDF parameters) derived every 8 days by inverting the model against MODIS multi-angular observations (cloud-cleared, atmospherically corrected surface reflectances) collected for each location within a 16-day period.
- 10 These kernel coefficients only depend on wavelength but not on illumination or observation angles, and have been provided globally in the MODIS gap-filled BRDF Collection 5 product MCD43GF (Schaaf et al., 2002, 2011).

- 15 Over water surfaces (including inland waters and oceans), light specularly reflected from a rough water surface as well as diffuse light backscattered by bulk water and transmitted through the water surface are considered. Reflection from the water surface is described by the Cox-Munk slope distribution function as implemented in Mishchenko and Travis (1997). A Case 1 water model

(Morel and Gentili, 1996) that has chlorophyll concentration as a single input parameter is applied to account for water-leaving radiance (i.e., light backscattered by water column into the atmosphere) including directionality of the underwater diffuse light. Chlorophyll concentration, wind speed, and wind direction are the only model input parameters.

5 ~~Since the~~ focus of this paper is on evaluating the derived GLER over land surfaces (pixel land fraction ≥ 0.99). ~~However, for completeness, details on ocean models are given in Appendix ??.~~ ~~, the brief description of the ocean models here is only for completeness. Details on water BRDF models and input datasets for wind speed and direction as well as chlorophyll concentration will be provided in a separate paper for ocean GLER validation.~~ ~~!htFlowchart of the GLER processes.~~
10 ~~Different colors stand for different data types/sources: grey for ancillary data for both land and water, purple for preprocessed input parameters or atmospheric input parameters, gold for sensor-dependent pixel-related inputs/output, and finally, blue ovals for the physical models used. All input data are represented by the rounded rectangles and output product is shown in the box rectangle. DEM denotes digital elevation model. RTLS denotes the Ross-Thick/Li-Sparse Reciprocal functions (see~~
15 ~~section 2.1 below for details). Also see Eq. 2 for definitions of I_0 , T and S_b and Appendix A for models used over water.~~

2.2 ~~Kernel-driven~~ MODIS BRDF and land type products ~~product~~ for land surfaces ~~from MODIS~~

MODIS is a cross-track scanning radiometer and has 36 spectral bands ranging in wavelength from
20 0.4 μm to 14.4 μm . Two bands (1 and 2) have a nominal resolution of 250 m at nadir, with five bands (3 to 7) at 500 m, and the remaining 29 bands at 1 km. MODIS views the entire Earth surface approximately daily via a two-side scan mirror that provides a swath of 2330 km cross track by 10 km along track (at nadir) each scan. The MODIS instruments are operated onboard the National Aeronautics and Space Administration (NASA) Aqua and Terra satellites, which have 16-day repeat
25 cycles and provide measurements on a global basis every 1-2 days. MODIS data are used to study the oceans, atmosphere and land (Justice et al., 1998). The calibration uncertainty for MODIS band 3 is within 2% (Xiong et al., 2005). The MODIS Aqua solar reflective bands including band 3 were corrected for a time-dependent drift in Collection 5 (Wu et al., 2013) but errors in MODIS Terra of up to 5% across the scan developed approximately 5 years after launch and this error was not
30 sufficiently corrected in Collection 5 (Sun et al., 2014; Lyapustin et al., 2014).

To compute ~~GLERs~~GLER, we use Collection 5 MODIS BRDF/Albedo Product MCD43 for land surfaces (Sun et al., 2017; Schaaf et al., 2002, 2011). ~~This product uses the atmospheric-corrected~~ The BRDF data in MCD43 is retrieved from surface reflectance data ~~(in the MODIS Collection 5 MOD09) from MODIS instruments on both Aqua and Terra satellites (Vermote and Kotchenova, 2008).~~
35 ~~Atmospheric correction has been carried out based on the~~ product. The atmospheric correction is applied in the MOD09 product to cloud-free or partially cloud-contaminated pixels. The cloud

mask also reduces thin cirrus cloud contamination (Vermote and Kotchenova, 2008). The correction removes the effects of gas and aerosol absorption, aerosol scattering, and corrects adjacency effects caused by variation of land cover, surface and atmosphere coupling effects (Vermote et al., 2002, 2007, and 2008). The algorithm uses tables constructed with the 6SV (Second Simulation of a Satellite Signal in the Solar Spectrum, Vector(6SV, Vector) radiative transfer code (Vermote et al., 1997; Kotchenova and Vermote, 2007; ~~Vermote et al., 2002~~). The overall accuracy of surface reflectance varies with band and aerosol optical thickness using key input parameters such as aerosol properties (aerosol optical thickness, size distribution, refractive indices and vertical distribution), atmospheric pressure, ozone amount and water vapor content. Holben et al. (1998), Remer et al. (AOT)(Vermote et al., 2002). Under clear atmospheric conditions at band 3 (470 nm), the accuracy is 2005), and Gao and Kaufman (2003) describe these input data. The atmospheric correction for MODIS band 3 used in this study has a theoretical error budget of about 0.005 in reflectance unit as shown in Table 2 of Vermote and Kotchenova (2008). The relative error due to the Lambertian assumption on surface reflectance does not exceed 0.8% in the inter-model comparison (Kotchenova and Vermote, 2007), but could be much higher (e.g., 3-12% in the green band) when comparing to multiangular field measurements (Franch et al., 2013). reflectance units (Vermote et al., 2008). We note that the atmospheric correction neglects surface anisotropy and that Wang et al. (2010) and Franch et al. (2013) have found doing so can introduce a modest negative bias in the corrected surface reflectance product, but despite this, Roman et al. (2013) found MODIS BRDF/Albedo products met the absolute accuracy requirement of 0.02 for spring and summer months.

Since the morning overpass (Terra) and afternoon overpass (Aqua) view the same location with different Sun-viewing sun and viewing geometries, use of data from both satellites would double the angular samples during the 16-day repeat cycle and reduce, thus increasing the number of high quality, cloud-free observations, and reducing the uncertainty and random noise amplification of anisotropy retrievals (Schaaf et al., 2011). The kernel coefficients retrievals (Salomon et al., 2006; Schaaf et al., 2011). The absolute accuracy requirements for albedo for all bands in MCD43 product has been extensively validated is 0.02 in reflectance units or 10% of surface measured values (Jin et al., 2003; Roman et al., 2013). Indeed, the majority of the extensive validation campaigns on different platforms at different scales across different landscapes. Most of the validation efforts has focused on albedo validation of the product (Salomon et al., 2006; Knobelspiess et al., 2008; Liu et al., 2009; Roman et al., 2009; Wang et al., 2010). Two particular comparisons with airborne multiangle observations, the Cloud Absorption Radiometer (CAR) measurements (Roman et al., 2013) and the Airborne Hyperspectral Scanner (AHS) data (Sobrino et al., 2013), have demonstrated a very good agreement with the airborne images, and seasonal cycles have demonstrated that the MCD43 product meets this requirement. These include comparisons with ground-based or airborne measurements (e.g., Wang et al., 2004 in the Tibetan Plateau; Coddington et al., 2008 over Mexico city; Wang et al., 2012 in snow-covered tundra) as well as with space-borne data (e.g., Susaki et al., 2007 in paddy fields using Advanced Spaceborne

~~Thermal Emission and Reflection Radiometer (ASTER) and MODIS-derived estimates met the accuracy requirements established for the high-quality MODIS operational product when solar zenith angle (SZA) is less than 70°.~~

~~The kernel-driven BRDF model used in Enhanced Thematic Mapper Plus (ETM+) data; Roman et al., 2013 with Landsat and the MCD43 BRDF/Albedo algorithm is known as the Ross-Thick/Li-Sparse Reciprocal (RTLS). RTLS consists of a linear combination of the weighted sum of an isotropic parameter and two kernels of viewing and illumination geometry (Roujean et al., 1992). The Ross-Thick kernel is derived from radiative transfer models (Ross, 1981) for volume scattering within a dense vegetation canopy, and the Li-Sparse Reciprocal kernel is based on surface scattering and geometric shadow-casting with mutual shadowing theory (Li and Strahler, 1992). Cloud Absorption Radiometer (CAR) data; and Wang et al., 2014 using ETM+). However, there are a few cases where MODIS retrieved albedo are smaller than field measurements, e.g., a bias of -0.01 for the visible broadband albedo (0.3-0.7 μm) over FLUXNET tower sites (Cescatti et al., 2012; Wang et al., 2010).~~

~~The mathematical expression for the kernel-driven RTLS to estimate surface BRF is as follows:-~~

$$\text{BRF}(\lambda, \theta, \theta_0, \phi) = f_{\text{iso}}(\lambda) + f_{\text{vol}}(\lambda)k_{\text{vol}}(\theta, \theta_0, \phi) + f_{\text{geo}}(\lambda)k_{\text{geo}}(\theta, \theta_0, \phi),$$

~~where θ is the viewing zenith angle (VZA), θ_0 the solar zenith angle (SZA), and ϕ the relative azimuth angle (RAA). k_{vol} and k_{geo} are the Ross-Thick and Li-Sparse Reciprocal kernels; f_{iso} , f_{vol} and f_{geo} are the kernel weights (also called kernel coefficients or BRDF parameters) derived every 8 days by inverting the model against MODIS multi-angular observations (cloud-cleared, atmospherically-corrected surface reflectances) collected for each location within a 16-day period. MCD43 provides three kernel coefficients (f_{iso} , f_{vol} , and f_{geo} in Eq. 1) for 7 MODIS bands for snow-free land and permanent snow and ice cover every 8 days. The static land-water flag that is provided with MCD43 has same spatial resolution (30'') with eight surface categories.~~

~~Global characterization of BRDF from satellite measurements for surfaces covered by snow and ice is an area of active research.~~ Though recent improvements in the MODIS Collection 6 MCD43 BRDF data (Wang et al., 2018) may enable the use of the MCD43 data for seasonal and variable short-term snow cover in GLER product, the first version of the GLER product uses the gap filled (GF) Collection 5 product (MCD43GF) which is intended to provide BRDF parameters using the RTLS model for land surfaces free of seasonal snow and those covered by permanent snow or ice.

Other snow and ice BRDF models also exist, and, in fact, the calibration of the OMI instrument, described in ~~section 2.2~~ [Section 2.4](#), is based partly on an alternate model to describe reflectance from Antarctic ice (Jaross and Warner, 2008). Because validation of snow and ice reflectances is challenging and involves different issues than those of snow-free land, we plan to carefully evaluate the GLER product over snow and ice separately in a follow-on study using various sources of BRDF information. Until that time, the GLER product over snow and ice should be considered less mature than the BRDF over snow and ice free land, whether the snow and ice are permanent (using MCD43GF), or seasonal (using OMI-derived LER) as described in ~~section 4.~~ [Section 3](#).

To obtain kernel coefficients for a given OMI pixel, the collocated MCD43GF points within an OMI pixel FOV are averaged. ~~The pixel land fraction is estimated by converting the eight surface category map into a binary (see Appendix A1 for details). Since kernel coefficients depend on wavelength, for the present study we selected MODIS band 3, the shortest wavelength in the MCD43GF product, with a center wavelength of 470 nm (ranging from 459 to 479 nm) to represent 466 nm, which is the wavelength used in our cloud algorithm to retrieve effective cloud fraction (ECF) (Vasilkov et al., 2017). Observations at this wavelength are relatively free of atmospheric rotational-Raman scattering (RRS) and trace gas absorption.~~

2.3 Pixel land areal fraction

The areal fraction of land (or water) for each OMI pixel is a critical parameter in TOA radiance calculation for pixels mixed with land and water (see Eq. 3). However, it cannot be estimated from OMI L1b pixel surface category flags because these binary flags do not provide information on mixed pixels. Therefore, a binary land/water classification method is developed to estimate pixel land fraction from the high resolution (30", same as MCD43) static land-water mask, i. e., map provided with MCD43.

First, we convert the eight surface categories from MCD43 into a binary land-water flag, merging all shorelines and ephemeral water at the MODIS spatial resolution into the land category class and classifying all other water sub-categories simply as water. The areal fraction of land (or water) for each OMI pixel is then computed as the statistics of the binary categories, from the counts of land and water points within the OMI FOV. Typical results are shown in Figure 2. ~~Our approach of estimating the land area fraction provides for more accurate calculation of TOA radiances in mixed pixels (see Eq. 3) as compared with the use of the eight surface category flags in the OMI level 1b data set.~~ Accurate estimation of pixel land fraction is also very important because BRDF models for land and water surfaces are quite different (strong backward scattering over land vs strong forward scattering over water) with different wavelength dependence. In contrast with previous studies (e.g., Zhou et al., 2010), we apply the ocean models described in ~~Appendix ??~~ Section 2.1 to coastal zones and inland waters instead of using MODIS data, because the MODIS ~~kernel~~ kernel-driven BRDF model is not applicable for water surfaces. ~~h Pixel water fractions (color bar) estimated in GLER (left), MODIS 30" land-water map (middle), and OMI L1b pixel land-water category (right). The five-color legend denotes surface categories defined in the original MODIS or OMI L1b data. Top panel: region of Lakes Superior and Michigan; Bottom panel: Chesapeake Bay.~~

~~The above kernel coefficients depend on wavelength. For the present study we selected MODIS band 3, the shortest wavelength in the MCD43GF product, with a center wavelength of 470 nm (ranging from 459 to 479 nm) to represent 466 nm, which is the wavelength used in our cloud algorithm to retrieve effective cloud fraction (ECF) (Yang et al., 2015). Observations at this wavelength are relatively free of atmospheric rotational-Raman scattering (RRS) and trace gas absorption.~~

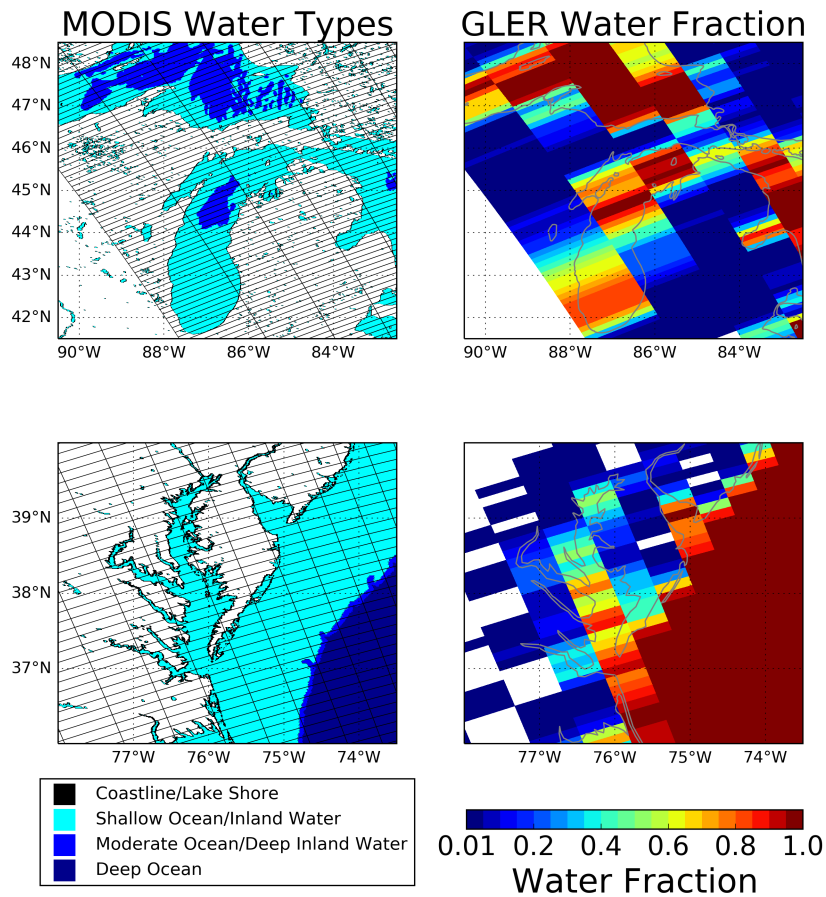


Fig. 2: Pixel water fractions (color bar) estimated in GLER (right) with MODIS 30'' land-water map (left) with OMI pixel polygons on the top. The color legend denotes surface categories defined in the original MODIS data. Top panel: region of Lakes Superior and Michigan; Bottom panel: Chesapeake Bay.

30 2.4 OMI data and selection criteria

OMI, launched onboard the NASA Aura satellite in July 2004, is a Dutch-Finnish hyper-spectral passive imager measuring in the 270-500 nm wavelength range with two CCD detectors (UV and Vis). It was designed to provide information about trace-gases, such as O_3 , NO_2 , SO_2 , HCHO, as well as absorbing aerosols. OMI has an instantaneous FOV of 0.8° in the flight direction (along-track) and 115° in the swath direction (cross-track), which yields an overall ground coverage of about 13 km by 2600 km at an altitude of 700 km. OMI measurements nominally provide daily global coverage with a $13\text{ km} \times 24\text{ km}$ resolution in the nadir position.

OMI collection 3 data are used in this study. Specifically, we use LERs-~~LER~~ retrieved from TOA

~~reflectances~~ radiances at 466 nm that are computed by normalizing the OMI radiances to the OMI day-1 solar irradiance spectrum measured on 21 December 2004 along with a correction for the Earth-Sun distance when calculating OMI-derived LER. The GLER product is designed to characterize the magnitude and the angular variability of the Earth’s surface reflectance ~~under~~ in a Rayleigh atmosphere, so in the context of GLER product validation, absolute radiometric response and consistency across the measurement swath are the two most critical aspects of instrument calibration to consider. For this study we ignore spectral dependence in the calibration, because our focus is strictly on the 466 nm channel. Spectral calibration will be important for validation of future versions of the GLER product that are planned to report data at several other wavelengths.

~~The OMI calibration has been detailed in previous work.~~ Dobber et al. (2008) estimated that the uncertainty in viewing angle dependence of OMI collection 3 sun-normalized radiances is less than 2%. ~~Their estimate follows the application of calibration adjustments based on the evaluation of TOA measurements over a target region of Antarctic ice, using a surface model that accounts for non-Lambertian effects in a radiative transfer model of the atmosphere as described by Jaross and Warner (2008). In that work, the authors used the same technique to establish the absolute radiometric calibration of OMI at nadir within an estimated model uncertainty of 1 and the radiometric calibration uncertainty is 2%.~~ Schenkeveld et al. (2017) evaluated long-term changes in the absolute radiometric response of the OMI instrument and estimated degradation of approximately 1-1.5% over the lifetime of the mission in the wavelength region used in this study.

Since only clear sky measurements are used for our comparison, we apply the UV aerosol index (AI) from OMAERUV product (Torres et al., 2007) to detect and screen out absorbing aerosol contaminated OMI measurements. This aerosol index is defined as the ratio of radiances measured at 354 and 388 nm compared to the ratio calculated for a pure Rayleigh-scattering atmosphere. It is sensitive to the presence of absorbing aerosols that reduce LER retrieved from OMI data. To screen out cloud contaminated pixels in the OMI measurements, we use ECF (~~effective cloud fraction~~) from the oxygen dimer ($O_2 - O_2$) cloud product algorithm described in Vasilkov et al. (2018). ~~The criteria we chose for data screening are~~ For this analysis, $|AI| < 1.0$ and $ECF < 0.02$. ~~We found that more stringent criteria than these removed too much data from the analysis, and that relaxation above these thresholds began to introduce 0.04 are used for cloud and aerosol contamination that noticeably degraded the results.~~ screening (see Appendix C for more details on cloud screen selection). Data with SZA greater than 70° are not included in this analysis as the MCD43 product does not recommend the use of data beyond 70° SZA.

35 2.5 Ancillary data sets

In order to produce the pixel-level GLER product, we need first to collocate and average ancillary data that have different spatial resolutions over the OMI FOV for the physical models that we use. Table 1 summarizes the ancillary data used in terrestrial GLER production along with their

spatio-temporal resolutions. This includes digital elevation model (DEM) data (ETOPO2v2) from the National Oceanic and Atmospheric Administration (NOAA). The ancillary data with higher spatial resolution than OMI are first ~~colocated~~ collocated with the OMI pixel using the so-called point-in-polygon methodology described by Haines (1994) and applied by Fisher et al. (2014) in the development of a merged OMI-MODIS cloud product. ~~An example to use this method to collocate the high-resolution MODIS BRDF product (MCD43GF) is shown in Figure ??.~~ Actually, ~~this collocation method can be applied to any kind of satellite pixel shapes.~~ ~~An illustration of collocating the high-resolution MODIS BRDF data with an OMI pixel FOV. Sample space is defined as the MODIS data space that encloses the entire OMI pixel polygon. N_{in} is the number of MODIS data points within the OMI pixel (red dots). Numbers at each pixel corner indicate its geolocation (longitude, latitude). Two pixels are selected: cross-track position 03 (near the edge of swath) and cross-track position 30 (near nadir) for orbit 12399 with along-track position 1000. An OMI pixel is defined with respect to the polygon formed by the four OMI pixel corner points, as described in the OMPIXCOR data product (see https://disc.gsfc.nasa.gov/datacollection/OMPIXCOR_003.html for more information).~~ OMPIXCOR provides two sets of coordinates 1) Non-overlapping and 2) Overlapping coordinates. We used the Vis channel overlapping coordinates, corresponding to 75% of the energy in the along-track field-of-view, as they are considered more accurate for scientific analysis than the non-overlapping coordinates that are provided mainly for mapping purposes. Additional ~~details~~ Details regarding the collocation and averaging of ancillary data sets are given in ~~Appendix A2~~ Appendix A1.

Table 1: Spatial and temporal resolutions of ancillary data used for land GLER calculation

Name	Source	Spatial	Temporal
DEM	ETOPO2v2/NOAA	2'	N/A
Land-water flag	MODIS	30''	N/A
Land BRDF parameters	MCD43GF/MODIS	30''	8 days

2.6 GLER computation

Given all necessary input parameters, TOA radiances (I_{comp}) are computed with the Vector Linearized Discrete Ordinate Radiative Transfer (VLIDORT) model. VLIDORT is a vector multiple scattering radiative transfer model that can simulate Stokes 4-vectors at any level in the atmosphere and for any scattering geometry with a Lambertian or non-Lambertian underlying surface (Spurr, 2006). ~~VLIDORT has the ability to simulate attenuation of solar and line-of-sight paths in a spherical atmosphere. In this study, we consider the sphericity correction for both incoming solar and outgoing viewing directions based on a regular~~ In this study, VLIDORT computations are carried out using the pseudo-spherical geometry calculation. ~~This is important for large solar and viewing zenith~~

angles. ~~We also consider polarization using the vector mode, because correction, i.e. for both~~
5 ~~multiple and single scattering calculations, solar beam attenuation (before scattering) is treated for~~
~~a spherical non-refractive atmosphere. Multiple scatter calculations are done for a plane-parallel~~
~~medium. However, in the single scattering treatment, both solar-beam and line-of-sight attenuations~~
~~are computed for a spherical-shell atmosphere. These “sphericity corrections” are necessary to~~
10 ~~obtain the most accurate results for geometrical configurations with large solar zenith angles, and~~
~~also for wide-angle viewing scenarios. VLIDORT is executed in vector mode for our calculations,~~
~~since neglect of polarization can lead to considerable errors for modeling backscattered spectra in~~
~~the UV/Vis wavelength range. The MODIS semi-empirical~~

~~We simulate clear sky TOA radiance (I_{comp}) over a non-Lambertian surface by coupling VLIDORT~~
~~with the MODIS kernel-driven BRDF function is selected (Eq. 1) from the group of analytical BRDF~~
15 ~~models available in the VLIDORT BRDF supplement. This surface BRDF supplement is a separate~~
~~module from the VLIDORT main program and can be upgraded by adding new analytical BRDF~~
~~models as needed.~~

~~to account for the surface BRDF effect on TOA radiance over land surfaces.~~ Then GLER (or
simply R) is defined and derived by inverting

$$20 \quad I_{\text{comp}}(\lambda, \theta, \theta_0, \phi, P_s, \text{BRF}_s) = I_0(\lambda, \theta, \theta_0, \phi, P_s) + \frac{RT(\lambda, \theta, \theta_0, P_s)}{1 - RS_b(\lambda, P_s)}, \quad (2)$$

where P_s is the pressure at the reflecting surface, I_0 is the path scattering radiance by the atmosphere,
calculated as the TOA radiance for a black surface, T is the transmitted radiance, i.e., incident total
(direct + diffuse) irradiance multiplying by transmittance from TOA to the reflecting surface along
the incoming solar beam as well as that from the surface to TOA along the satellite view direction,
25 and S_b is the diffuse flux reflectivity of the atmosphere, i.e., the fraction of upward radiance from
the surface scattered back to the surface by the atmosphere (Dave, 1978). All angles are defined as
in Eq. 1. The input surface BRDF (i.e., BRF_s) to VLIDORT is simulated either with Eq. 1 over land
or with models described in ~~Appendix ??~~ Section 2.1 over water.

~~We also computed I_0 , T and S_b with VLIDORT by calculating TOA radiances for three values~~
30 ~~of R , and then solving three linear equations in the form of Eq. 2 to derive the three terms.~~ To
speed up computations, however, we created lookup tables of the quantities I_0 , T and S_b for dif-
ferent ~~Sun-viewing~~ sun and viewing geometries and for a number of surface pressure levels (see
Appendix B for details). Note that Eq. 2 can also be used to derive LER directly from satellite ob-
servations by simply replacing the computed TOA radiance (I_{comp}) with observed TOA radiance
35 (I_{obs}). This approach is used in Section 3, where we compute and compare OMI-derived LER to
VLIDORT-simulated GLER for validation.

~~To calculate TOA radiance with VLIDORT on a pixel basis~~ To make the simulated TOA radiance
more realistic to a given pixel geolocation, we construct dynamical atmospheric optical property pro-
files using the surface (terrain) pressure, temperature and their profiles pixel by pixel. The pressure
profile is then generated following Lagrangian control volume (LCV) coordinate system starting

from the surface pressure (see discussion in Appendix A2). The temperature profile is based on the
 5 Global Modeling Initiative (GMI, see Rienecker et al. (2011)) monthly climatological temperature
 profiles. Finally, we calculate the layer total optical thickness and single scattering albedo following
 Bodhaine et al. (1999) for Rayleigh cross-section calculation. Compared with the static profiles used
 previously (e.g., Vasilkov et al., 2017), these dynamic atmospheric profiles better represent the actual
 Rayleigh atmosphere above the OMI pixel and result in a more accurate TOA radiance simulation.
 10 This dynamic profiles only apply to online calculations, whereas for this work the static profiles
 approach is used for look-up table (LUT) construction.

For uniform surface pixels (either 100% land or water), we calculate TOA radiance by coupling the
 surface anisotropy models specified in Section 2.2 (for land) or Appendix ?? (for water) Section 2.1
 with VLIDORT. For heterogeneous surface pixels (i.e., mixed with land and water), the TOA radi-
 ance is estimated using an (I_{comp}) is estimated following the independent pixel approximation, i.e.,
 using the area-weighted radiance for uniform from both land (I_{land}) and water (I_{water}) contributions
 within an OMI FOV, i. e., replacing I_{comp} in Eq. 2 with as follows.

$$5 \quad I_{comp}^{TOA} = f_L I_{land}^{TOA} + (1 - f_L) I_{water}^{TOA}, \quad (3)$$

where f_L is the pixel land fraction, estimated as described in Section 2.2.3. Figure 3 shows exam-
 ples of I_{land}^{TOA} , I_{water}^{TOA} and I_{comp}^{TOA} .

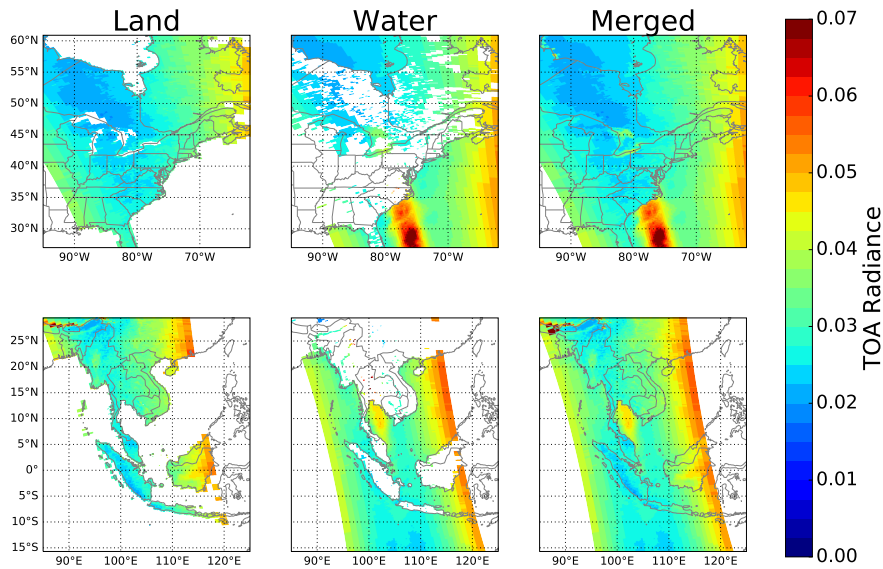


Fig. 3: Pixel-based simulated TOA radiance over land (left) when the pixel land fraction is larger
 than 5%, water (middle) when the pixel water fraction is larger than 5%, and the merged scene using
 Eq. 3 (right). Top panel: North America; Bottom panel: SE Asia.

It should be noted that aerosols are not included in the computation of the GLER. Scattering by aerosols in the atmosphere reduces the BRDF effects (Noguchi et al., 2014). Therefore, the use of the GLER may result in overestimation of the BRDF effects in the presence of aerosol and thin clouds. Our use of a retrieved ~~effective cloud fraction (ECF~~ that implicitly accounts for the effects of non-absorbing aerosol) will help to alleviate this problem (Boersma et al., 2011; Lorente et al., 2018; Vasilkov et al., 2018). We plan to examine aerosol effects on GLER in a future work.

3 Results

First, we examine the overall performance of GLER by comparison with the OMI-derived LER. ~~OMI-derived LER (i.e., which is calculated by solving for R in Eq. 2) is calculated by solving this equation, replacing the left term I_{comp} with OMI-measured TOA radiance as input for I_{comp} and other quantities (at 466 nm. We accounted for the small $\text{O}_2\text{-O}_2$ and O_3 absorption at 466 nm when computing the quantities I_0 , T and S_b) from lookup tables, as described in Section 2.4, for a given pixel's Sun-viewing geometry. When computing GLER, this was not necessary because these gases were not included in the simulation of the TOA radiances or the LUTs used to derive GLER. These I_0 , T , and S_b LUTs are interpolated with the sun and viewing geometry and surface pressure of a given pixel when calculating OMI-derived LER.~~ Then we carry out an in-depth evaluation over nine typical landscapes (see Table ??2 and Figure ??4) covering seasonal, interannual, and cross-track variations.

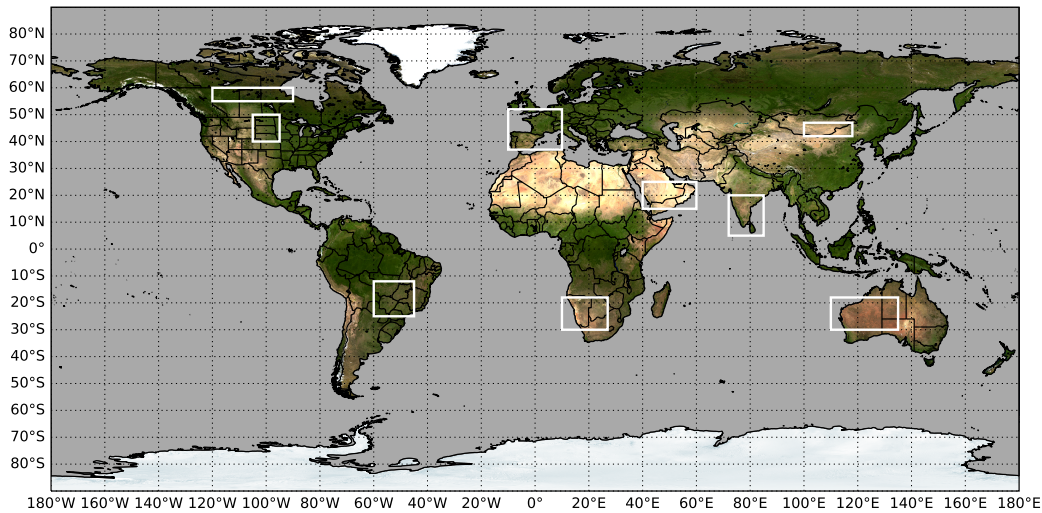


Fig. 4: Locations of selected geographical regions as specified in Table ??2

Table 2: Selected geographical regions for analysis

Region	Land Type	Longitude Range	Latitude Range
central Canada	Boreal Forest	120W-90W	55N-60N
central United States	Cropland/Grassland	105W-95W	40N-50N
southern Brazil	Cropland	60W-45W	25S-12S
Spain/France	Cropland/Forest	10W-10E	37N-52N
Arabian Desert	Barren	40E-60E	15N-25N
southern Africa	Open Shrubland	10E-27E	30S-18S
southern India	Crop Mosaic	72E-85E	5N-20N
Mongolia	Barren/Desert	100E-118E	42N-47N
western Australia	Open Shrubland	110E-135E	30S-18S

3.1 Overall performance

Figures ?? ?? show Figure 5 shows comparisons of GLER with clear-sky OMI-derived LER at 466 nm across various geographical regions for ~~different seasons in~~ 2006. The absolute LER varies ~~between greatly between the geographic~~ regions; for example, forested regions ~~have lower LER~~,
 10 ~~and deserts have higher LER~~ exhibit LER less than 0.05 while the LER of the deserts reach nearly 0.30. Overall, the OMI-derived LER is generally higher compared with the calculated GLER, as the ~~majority of the scatterplots have negative y-intercepts. There are several possible reasons for the differences, such as some background non-absorbing aerosols that slightly increase the OMI-derived reflectivity and small calibration differences between MODIS and the OMI instruments~~ distribution of data fall below the 1:1 line. While this bias does seem fairly consistent from region to region, there is some small change in the magnitude. Similar to Figure ?? but for a) southern Brazil; b) southern
 5 ~~India; and c) western Australia. Similar to Figure ?? but for a) southern Africa; b) Mongolia; and c) Arabian Desert.~~

Despite this small bias, we note that ~~$r^2 > 0.8$ for most~~ r^2 is greater than 0.8 for several of the regions, with the poorest agreement in darker regions such as southern Brazil and central Canada. ~~The brighter regions such as Mongolia and the Arabian desert exhibit excellent agreement with $r^2 > 0.9$.~~
 It is possible that in these ~~regions the enhanced brightness~~ darker regions where the agreement worsens, the darkness of the surface ~~minimizes~~ maximizes the impact of residual aerosols and clouds ~~. The comparison has the largest seasonal variation in regions where vegetation changes the that were~~
 5 ~~not completely removed from the OMI measurements. As seen in Table 3, the agreement varies the~~ most through the year in regions with large changes in vegetation, such as in southern Brazil where r^2 varies from 0.34 to 0.54. The desert regions such as the Arabian Desert show little to no change with season with r^2 only varying between 0.85-0.91. Overall we note that GLER is biased low when compared to OMI-derived LER by 0.01-0.02, with the largest bias over darker regions where we

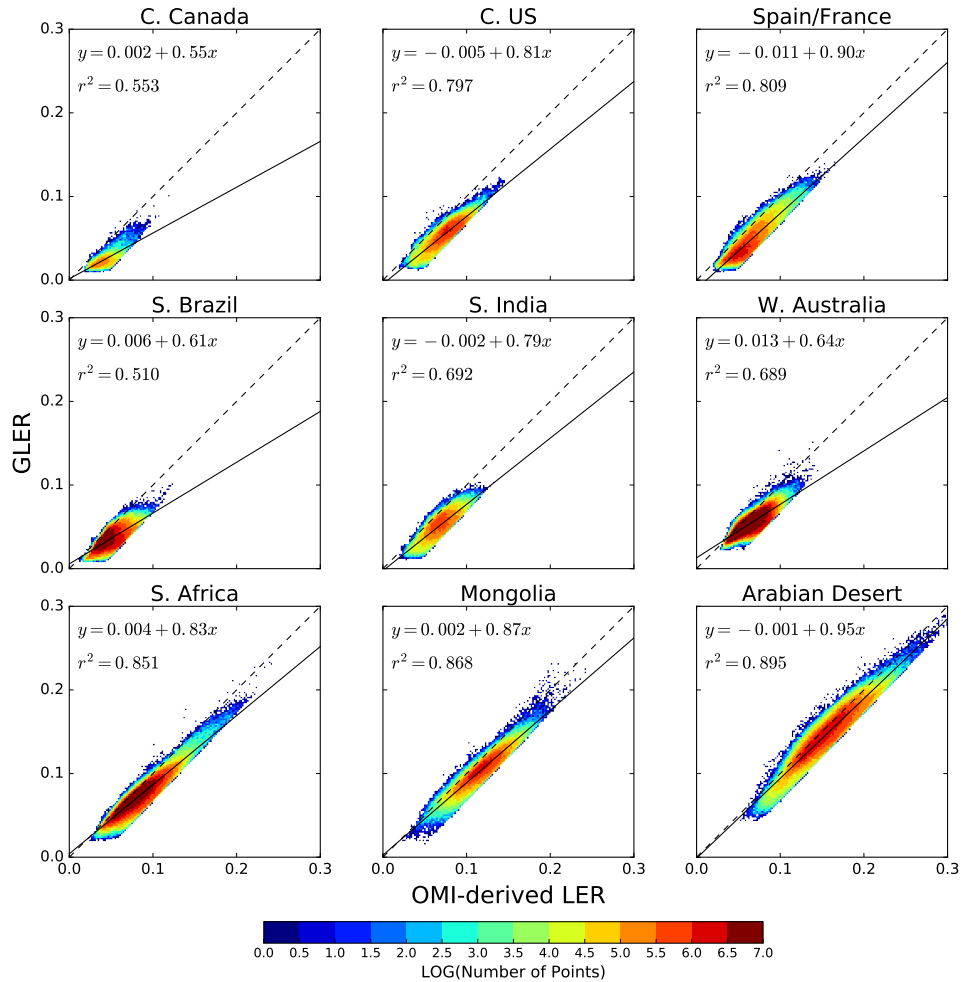


Fig. 5: Comparison of ~~aerosol~~aerosol and cloud cleared OMI-derived LER at 466 nm and GLER for ~~four seasons of 2006~~ across a) ~~central Canada~~; b) ~~central US~~; and c) ~~Spain/France~~various geographical regions. In the color-bar legend, N is the number of comparisons.

- 10 believe residual aerosols and clouds may play a larger role in brightening the OMI measurements. As mentioned in Appendix C, the mean of the GLER and OMI-derived LER difference may include some contribution from residual aerosol and cloud given the ECF screen used for the analysis. ~~In the Mongolia region there is a portion of data with GLER greater than OMI-derived LER during the winter months; it is possible that this is due to snow contamination in the MODIS BRDF data (Riggs et al., 2016).~~

3.2 Seasonal variations

Table 3: Seasonal Analysis of GLER

<u>Region</u>	<u>DJF</u>		<u>MAM</u>		<u>JJA</u>		<u>SON</u>		<u>Total Count</u>
	<u>Diff</u>	<u>r²</u>	<u>Diff</u>	<u>r²</u>	<u>Diff</u>	<u>r²</u>	<u>Diff</u>	<u>r²</u>	
<u>C. Canada</u>	<u>N/A</u>	<u>N/A</u>	<u>-0.015</u>	<u>0.61</u>	<u>-0.015</u>	<u>0.40</u>	<u>-0.017</u>	<u>0.56</u>	<u>20,865</u>
<u>C. United States</u>	<u>-0.019</u>	<u>0.40</u>	<u>-0.022</u>	<u>0.78</u>	<u>-0.019</u>	<u>0.79</u>	<u>-0.017</u>	<u>0.71</u>	<u>91,293</u>
<u>S. Brazil</u>	<u>-0.020</u>	<u>0.43</u>	<u>-0.014</u>	<u>0.34</u>	<u>-0.013</u>	<u>0.50</u>	<u>-0.014</u>	<u>0.54</u>	<u>197,732</u>
<u>Spain/France</u>	<u>-0.020</u>	<u>0.75</u>	<u>-0.017</u>	<u>0.71</u>	<u>-0.014</u>	<u>0.84</u>	<u>-0.019</u>	<u>0.83</u>	<u>131,959</u>
<u>Arabian Desert</u>	<u>-0.009</u>	<u>0.90</u>	<u>-0.007</u>	<u>0.88</u>	<u>-0.007</u>	<u>0.85</u>	<u>-0.009</u>	<u>0.91</u>	<u>299,860</u>
<u>S. Africa</u>	<u>-0.012</u>	<u>0.86</u>	<u>-0.010</u>	<u>0.87</u>	<u>-0.010</u>	<u>0.81</u>	<u>-0.011</u>	<u>0.82</u>	<u>379,898</u>
<u>S. India</u>	<u>-0.016</u>	<u>0.66</u>	<u>-0.019</u>	<u>0.67</u>	<u>-0.022</u>	<u>0.72</u>	<u>-0.022</u>	<u>0.60</u>	<u>78,156</u>
<u>Mongolia</u>	<u>-0.016</u>	<u>0.87</u>	<u>-0.012</u>	<u>0.83</u>	<u>-0.014</u>	<u>0.89</u>	<u>-0.013</u>	<u>0.85</u>	<u>142,770</u>
<u>W. Australia</u>	<u>-0.011</u>	<u>0.61</u>	<u>-0.009</u>	<u>0.67</u>	<u>-0.009</u>	<u>0.75</u>	<u>-0.007</u>	<u>0.66</u>	<u>161,123</u>

While surface BRDF does not change Surface BRDF or albedo change is small on a day-to-day basis, there is variability in the BRDF with the exception of extreme events such as fires and floods which may not be captured with the 16 day MODIS dataset (Schaaf et al., 2011). There is, however, noticeable variability in BRDF and albedo between seasons due to land cover changes throughout the year. Since the MODIS BRDF model parameters are calculated every 8 days, they capture the changes in BRDF can capture the BRDF and albedo changes from season to season over various land cover types. Figure ??-6 shows the seasonal variability of LER from model simulations GLER, Kleipool Climatology, and OMI-derived LER for various land cover types in 2006 for cloud and aerosol free pixels that have been screened for clouds and aerosols. Comparisons of OMI reflectivity data with GLERs in the central Canada region are excluded GLER show little data across central Canada in the winter months due to the presence of seasonal snow cover, while in the southern India region, missing data occur due to persistent cloud cover during the monsoon season in the summer months.

Throughout the year, both GLER and OMI-derived LER vary as much as 0.03-0.04 at 466 nm. The GLERs follow due to changes in vegetation. The GLER follows a similar seasonal variation as compared with the OMI-derived LER with an absolute difference of 0.01. In the Arabian region the -0.02. We note that while the bias varies by region, there is little to no variation of the bias through the year in each individual region. The greatest agreement between GLER and the OMI-derived LER and GLER data agree very well appears to be in the Arabian region possibly because the background aerosols in this high reflectance region have less impact than in other regions due to the brightness of the surface. The Kleipool et al. (2008) LER data (monthly LERs interpolated at 470 nm are used here) exhibit seasonal variations in the various geographic regions but the seasonal variability does not closely follow the exhibit the general seasonal variations seen in the OMI-derived LER but to a smaller magnitude. This is seen well in the southern Africa region where the Kleipool data show

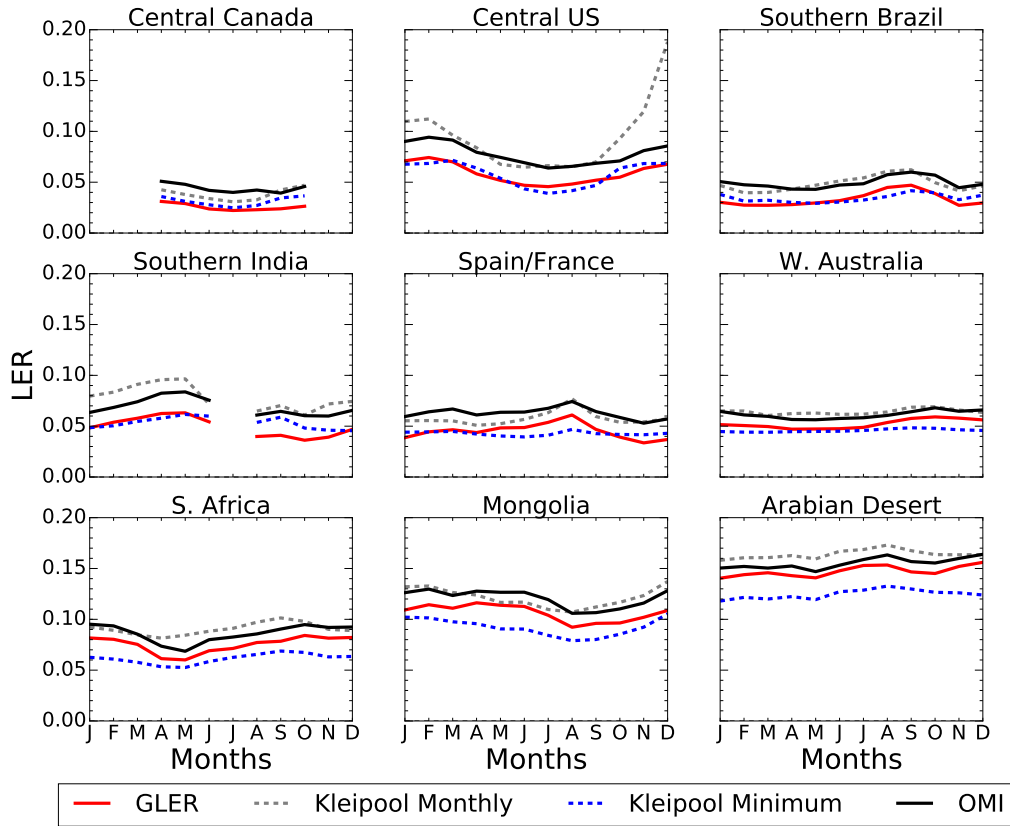


Fig. 6: Seasonal dependence in 2006 of GLER (solid red), Kleipool et al. (2008) monthly climatological LER (dashed grey), Kleipool et al. (2008) minimum climatological LER (dashed blue) and OMI-derived LER (solid black) at 466 nm.

a yearly minimum in March, whereas the OMI-derived LER, possibly because of cloud and/or aerosol contamination and GLER show the yearly minimum LER occurring closer to May. This could be due to the fact that the Kleipool data do not capture the variability that could occur year to year due to drought or anomalous rainy periods. In the winter months across the Central US, the Kleipool et al. (2008) data agree less well with the OMI-derived LERs, possibly due to the presence of contamination from seasonal snow or clouds in the climatological dataset.

3.3 Interannual variations

When comparing results of calculated GLER against OMI-derived LER, it is important to compare data from multiple years in order to determine whether factors such as land type changes or satellite calibration drifts have an impact on the evaluation. After 2007, OMI radiances in some rows or cross-track positions are affected by an anomaly that occurred outside the instrument, producing a blockage of the intended FOV and/or scattered sunlight from outside the FOV for some rows of the CCD detectors. This is known as the OMI row anomaly, and it affects all wavelengths to some

degree (see <http://projects.knmi.nl/omi/research/product/rowanomaly-background.php> for more information). We therefore limit the year-to-year analysis to rows 1-20 that are not impacted by the row anomaly. We also greatly minimize the impact of snow and ice ~~mis-classification~~ misclassification and sub-pixel contamination by restricting our comparison to land surfaces below latitudes of 60°.

10 January and July calculated ~~GLERs are~~ GLER is compared with OMI-derived ~~LERs~~ LER for 2006 and 2015 in Figure ~~???~~ 7. Similarly to ~~Figures ??-??, at lower LER values~~ Figure 5, the GLER values are generally biased low compared with the OMI-derived ~~LER is biased slightly high compared with~~ GLER, but for higher LER values GLER and OMI-derived LER are in excellent agreement with a y-intercept of around -0.015 in Figure 7. There are some outliers where GLER is significantly
15 higher than the OMI-derived LER. ~~This is caused by localized flood plains that appear darker after rain but quickly dry up in a day or two which the MODIS data do not capture this very small scale temporal variability.~~ The good agreement between These data are from the Salar de Uyuni salt lake in southwest Bolivia and Lake Frome in southern Australia which only fills up during heavy rain events. These lake basins typically retain water for short periods of time and likely would not be captured in the 16 day MODIS BRDF data (Schaaf et al., 2011). The agreement of GLER and OMI-
5 derived LER ~~does not change with season (January vs July) and year (is quite similar for 2006 vs and 2015), as all plots have identical intercept values and the variability in the slope is at most 0.03.~~ with only a small increase of the slope for July 2015 as compared to July 2006.

Figure ~~??~~ 8 shows a fairly constant bias between GLER and the OMI-derived LER ~~is smallest for brighter surfaces, whereas the difference gets larger as the~~ surface becomes darker. This agrees with earlier figures and could be caused by higher efficiency of scattering aerosols over darker surfaces than brighter surfaces due to decreased solar radiation being reflected from the darker surface. GLER is smaller than OMI-derived LER because of residual cloud contamination in the OMI data that is not completely screened out., with the exception being at lower LER's where the bias decreases possibly due to the darkening of OMI LER from to
10 shadowing from large clouds at high latitudes (Zhu et al., 2012). The differences in the July data between 2006 and 2015, though a little bit larger than those in the January data, are still within the calibration uncertainties. ~~Also in July the differences are smaller in 2015 than 2006 until LER reaches 0.20. But given the~~ Given the magnitude of the difference ~~this could be,~~ while it could be caused by some satellite degradation, it is possible that it could be attributed to sampling differences
15
20 due to aerosol or cloud variability.

3.4 Cross-track dependence

Figure ~~??~~ 9 shows LER dependence on the cross-track position across several regions with varying land types. There are two main factors that contribute to the cross-track anisotropy of LER. First and foremost is the BRDF effect. The second factor is the spatial heterogeneity of land coverage within
5 a selected region (box) that causes a nonuniform distribution of the surface reflectivity. This effect

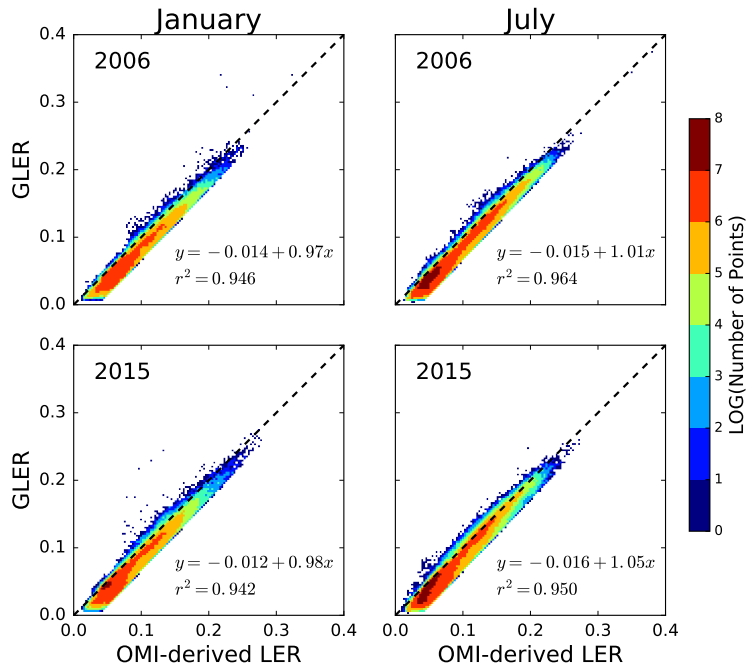


Fig. 7: Scatterplots comparing GLERs GLER with OMI derived LERs LER at 466 nm in January and July in 2006 and 2015, limited to rows 1-20 to exclude OMI data affected by the row anomaly. Latitudes are restricted to those below 60° to avoid introducing complications of snow/ice misclassification in the comparison.

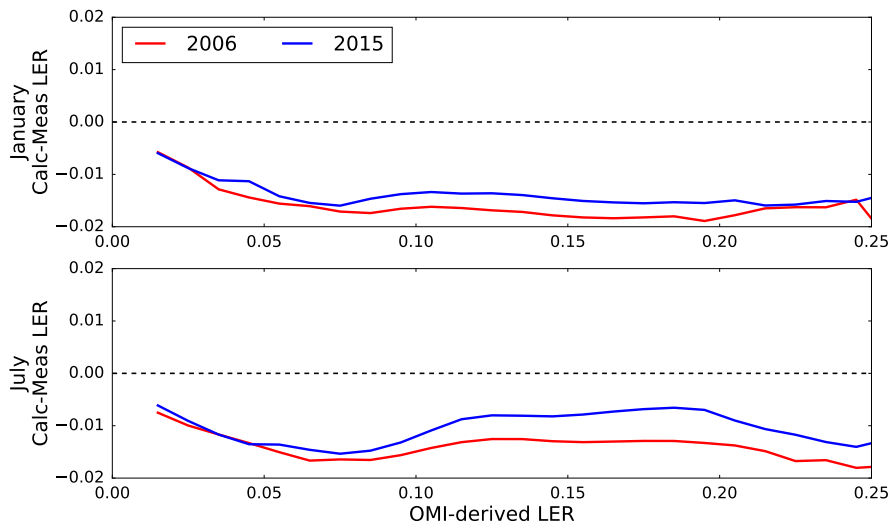


Fig. 8: Differences between calculated GLER and derived OMI LER at 466 nm plotted as a function of OMI derived LER in 2006 and 2015. Data were selected in the same way as those in figure [???](#).

is exaggerated for much larger pixels at the swath edges, as compared with those nearer to the nadir. We try to minimize the second effect by selecting the most uniform regions with sufficient numbers of pixels.

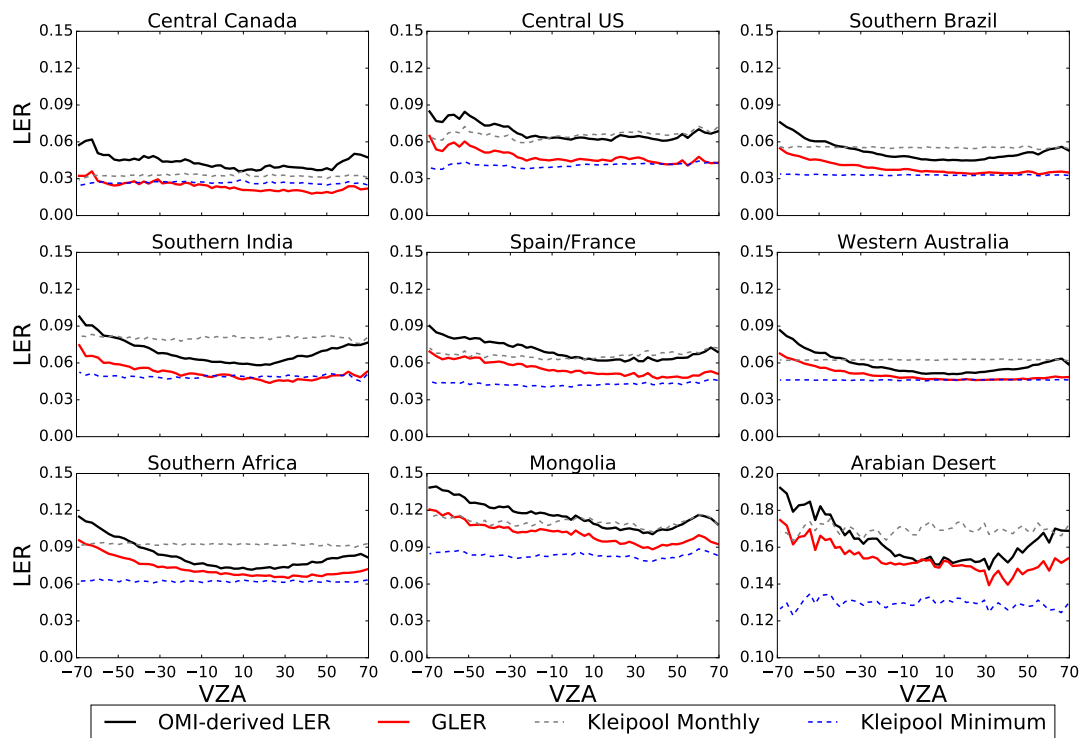


Fig. 9: Cross-track (or VZA) dependence of OMI-derived LER (black line), GLER (red line), and Kleipool et al. (2008) climatological LER (dashed line) for June-August 2006 (December-February 2006 in southern India) across various geographical regions screened for clouds and aerosols. Positive (negative) VZAs denote forward (backward) scattering directions.

However, as one can see from Figure ??9, even the Kleipool et al. (2008) climatology, which has no dependence on viewing geometry, shows variations with cross-track position due to spatial nonuniformity of the surface reflectivity for some regions such as Spain/France, Mongolia, and the central US. Due to the BRDF effects, OMI-derived LERs are generally larger further off nadir, in backward scattering directions. The GLER data exhibit a similar dependence, with highest values at the largest VZAs. In several of the brighter regions, we note that the regions that include strong absorbing dust aerosols such as the Arabian desert and western Australia, we note that the GLER is closer to the Desert and Western Australia compare well with the OMI-derived LER near nadir, with a small bias far at nadir but there is a bias further off nadir. This could possibly be the BRDF affect from the aerosols in these regions which are not modeled with GLER since it is assumed that there is an aerosol free Rayleigh atmosphere. The darker and more forested regions such as central Canada do not exhibit the same structure in the bias as a function

of cross-track dependence.

3.5 Sub-region case study

To further assess the anisotropy in GLER, we performed a small case study on a sub-region in western Australia (see Figure ??10) with very homogeneous land type and elevation. Figure ??11b shows that for this sub-region f_{iso} , which is a measure of the surface albedo, is very consistent for all rows due to the homogeneity of the surface. Figure ??11a confirms the homogeneity of this region as the Kleipool et al. (2008) climatological LERs are LER is nearly constant for all cross-track positions. We note that $f_{vol} * k_{vol}$, which is a measure of the scattering of leaves and background soil/sand particulates in the scene, increases towards the edge of the swath due to increased multiple-scattering. The shadowing effect (i.e., $f_{geo} * k_{geo}$) has similar cross-track dependence in backward scattering directions, although somewhat smaller. As seen in Figure ??11a, there is a similar pattern in the other regions (Figure ??9). In this case study, we note that the bias becomes larger towards the edge of the swath, possibly due to the longer path length allowing for a greater impact from isolated clouds or background aerosols. Nevertheless, the overall cross-track pattern is very similar between the OMI-derived LER and the calculated GLER.

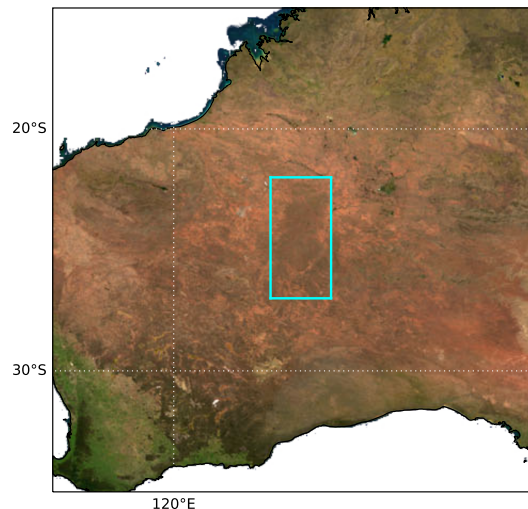


Fig. 10: Map of sub-region in western Australia with homogenous-homogeneous land type used in a case study.

4 Discussion

Vasilkov et al. (2018) reported that values of cloud fractions derived using GLERs-GLER in place of climatological LERs-LER are about 0.02 larger on average, and using GLERs-GLER can significantly enhance tropospheric NO₂ vertical columns in polluted regions through reduction of the

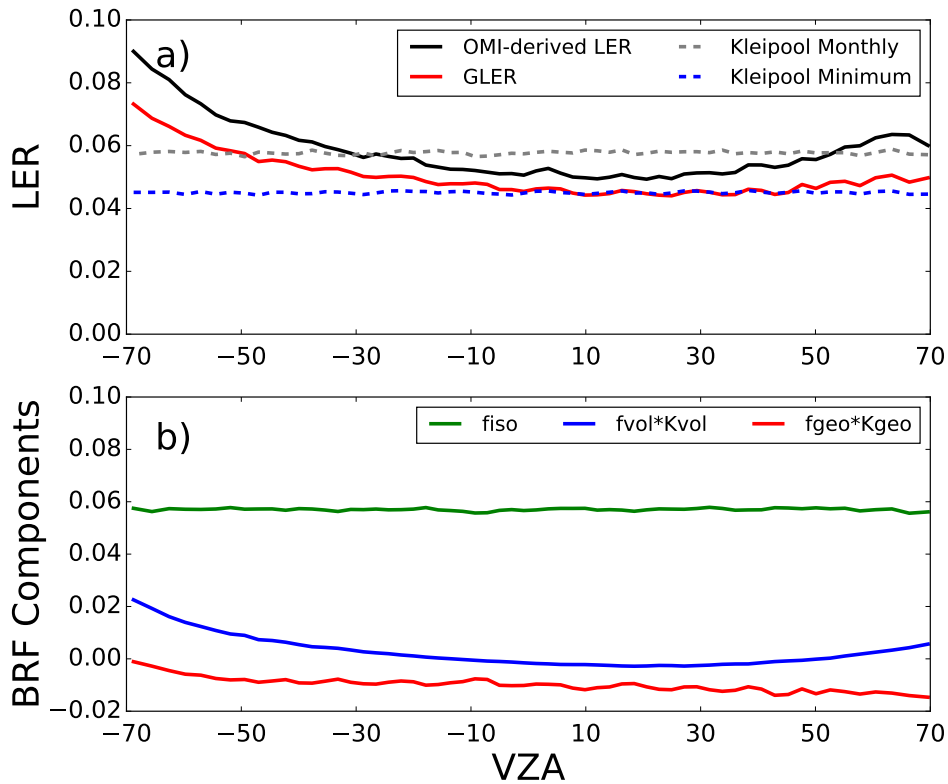


Fig. 11: Case study of cross-track (or VZA) dependence for a sub-region in western Australia in June-August 2006. a) 466 nm ~~LERs~~LER; b) BRF components from MODIS data. Positive (negative) VZAs denote forward (backward) scattering directions.

tropospheric air-mass factor (AMF). The results presented in Section 3 are therefore important as they demonstrate that the GLER concept as implemented with MODIS data is able to capture reliably the complex angular, seasonal, and inter-annual variations in OMI reflectances over different regions on the Earth with diverse land cover types.

10 A significant issue related to the GLER evaluation is the presence of thin clouds and non-absorbing aerosols over land surfaces. Both effectively result in the OMI-retrieved ~~LERs-data~~LER being larger than the calculated ~~GLERs~~GLER, since neither was included in the radiative transfer simulations. Here, we excluded data with elevated cloud fractions to mitigate cloud and aerosol effects. However, the fact that OMI-derived ~~LERs-are~~LER is consistently biased high by ~ 0.01 relative to
 15 ~~GLERs-0.02 relative to GLER~~ suggests that a certain amount of contamination is unavoidable. The effects of aerosols are partially accounted for indirectly through the current cloud algorithms that do not distinguish between clouds and non-absorbing aerosol. It is therefore important that the same approach to account of surface effects, whether it be the use of climatological LER or GLER, be used for both cloud and trace-gas retrievals.

5 In addition to background non-absorbing aerosol and/or residual cloud contamination, ~~this bias~~

it is important to consider that the GLER-LER bias may be due ~~to small calibration differences between~~ in part to differences in the MODIS and OMI radiance calibration. Sensitivity analysis of Eq. 2 used to compute LER and GLER shows that a 1% error in TOA radiances will produce errors in LER of up to 0.003 in surface reflectivity. A bias of 0.01 between GLER and LER requires a difference in MODIS and OMI ~~radiance of at least 3% for brighter land scenes (LER >= 0.2), and differences of 10% for darker land scenes (LER <= 0.05). MODIS TOA radiances would thus have to be 3-6% low relative to OMI to explain the bias seen in GLER-LER for bright scenes, and 10-20% low for dark scenes.~~

Jaross and Warner (2008) compared TOA reflectances from OMI and MODIS with radiative transfer model simulations over Antarctica, accounting for the BRDF of the snow surface. By indirect comparison, OMI Collection 3 and MODIS Collection 5 agreed to within 1% at the start of the OMI mission. They estimated the uncertainty of their technique is 2%. This level of disagreement is smaller than needed to explain all of the 0.01-0.02 bias of GLER over dark scenes. We therefore conclude that only some of the bias can be attributed to calibration differences. Additional information about the relative calibration of OMI and MODIS is provided in Appendix D.

Relative sensor drift is also a concern in comparing the GLER product using the MODIS calibration with LER from OMI. Aqua MODIS appears to be well corrected in Collection 5 but the MCD43 product also uses data from the Terra instrument, which has degraded appreciably over the lifetime of the mission. However, we find no evidence of time dependent change in Collection 5 MODIS BRDF data. We suspect the time-dependent and scan angle-dependent error in the Collection 5 MODIS Terra calibration data have somehow been avoided. Since OMI drift has not been fully corrected, and the MODIS drift has been removed (or avoided in the case of Terra, apparently) the slight decrease of OMI LER relative to GLER between 2006 and 2015 in figure 8 may be due to the 1-1.5% calibration drift in OMI radiances.

~~Despite~~ these factors that introduce ~~some~~ uncertainty into our evaluation, we conclude that the GLER product agrees remarkably well with the OMI measurements in largely clear-sky conditions.

Our results suggest that ~~GLERs~~ GLER may be used with confidence in OMI trace gas retrievals, many of which presently utilize climatological OMI LER data. However, it should also be understood that use of ~~GLERs~~ GLER calculated from aerosol-corrected MODIS BRDF data removes the effects of non-absorbing aerosols that are known to exist in the climatological LER data derived from UV/Vis sensors; this is supported by the slightly elevated OMI-derived ~~LERs~~ LER we find compared with ~~GLERs~~ GLER. ~~The effects of aerosols are partially accounted for indirectly through the current cloud algorithms that do not distinguish between clouds and non-absorbing aerosol. It is therefore important that the same approach to account of surface effects, whether it be the use of climatological LERs or GLERs, be used for both cloud and trace-gas retrievals.~~

There are other issues to be considered with the MODIS BRDF model and the Collection 5 gap-filled BRDF parameters (MCD43GF) over seasonal snow cover or permanent ice. The fact that

MCD43GF only provides snow-free land BRDF parameters usually leads to either data gaps or too small GLER values for snow-covered OMI pixels. The current temporary fix to this issue is to use OMI-derived LER but capped by a constant snow albedo of 0.6 as suggested in the KNMI's daily OMI NO₂ (DOMINO) product (Boersma et al., 2011; McLinden et al., 2014) based on the Near-
10 real-time Ice and Snow Extent (NISE) flags (Nolin et al., 2005) in the OMI L1b data set. The second issue is that the current MODIS kernel model lacks a mechanism to deal with strong forward reflection over snow/ice. Finally, since the shortest wavelength in the MODIS BRDF product MCD43GF is 466 nm, it does not cover the shorter range of OMI blue and UV wavelengths. We plan to explore other BRDF products in the future that have more wavelengths and fewer data gaps. A good candidate is the Multi-Angle Implementation of Atmospheric Correction (MAIAC) data (Lyapustin et al., 2012). Compared to MCD43GF, MAIAC includes a shorter wavelength (412 nm) and provides
15 pixel snow fraction that can be used for snow and ice covered regions.

We have focused here on evaluation of land ~~GLERs~~GLER, because the GLER product is primarily targeted towards improvement of retrievals of trace gas pollutants such as NO₂ that are concentrated
20 over land. We recognize that our evaluation in this paper excludes several important land types, such as compact and dense urban areas, land that is close to water, and a combination of the two. It can be a challenge to collect substantial amounts of data over cities, due to their relatively small size in comparison to the large regions that are the subject of this study. Particulate pollution is also common in urban regions, where non-absorbing sulfate aerosols can interfere with the derivation of
25 LERs, thus making it difficult to validate GLERs with satellite data. These regions require further careful study using data from days when these regions are exceptionally clear. Given the importance of understanding the influence of surface reflectance on AMF calculations in highly polluted regions, we believe this work should be carried out in the future.

The validation results reported in this study apply to OMI and other sensors in similar low-Earth
30 orbits that collect measurements with similar geometries, such as ~~TropOMI~~TROPOMI, which has higher spatial resolution than OMI (7 km at nadir). In theory, the smaller pixel size of ~~TropOMI~~TROPOMI and other future sensors should enhance the ability to validate the GLER approach by enabling more complete cloud and aerosol clearing for regions with widespread but broken clouds that were specifically avoided in the present work.

35 Since MCD43 product is not recommended for solar zenith angles beyond 70° (Schaaf et al., 2011), it may not be applicable for some geostationary (GEO) satellite observations, for which such high solar angles will certainly occur. Instead, GEO instruments such as the Geostationary Operational Environmental Satellite (GOES) imagers may be needed to provide BRDF coefficients that apply to the different range of observing conditions relevant to the planned GEO UV/Vis spectrometers.
5

5 Conclusion

The GLER product has been developed to account for surface BRDF effects on the ultraviolet and visible cloud, trace-gas, and aerosol algorithms. In this paper, we have evaluated the GLER product over land using OMI measurements for a range of land cover types. We described the atmospheric
10 RT and surface BRDF models as well as the sources of data used in those models to produce our GLER product. Over land, the GLER product uses gap-filled Ross-Thick, Li-Sparse kernel BRDF parameters [MCD43GF](#) derived from MODIS measurements to capture the directional reflectance properties of the land surface.

We evaluated the GLER product over land by comparing it with OMI-derived [LERs](#) [LER](#) over several typical geographical regions focusing on three aspects: seasonal variations, interannual changes, and cross-track dependence. After data are screened to remove the effects of aerosol and cloud contamination, the MODIS-based [GLERs](#) [GLER](#) show very good agreement with OMI-derived [LERs](#) [LER](#), with correlation coefficients larger than ~~0.9 for a majority~~ [0.8 for some](#) of the selected regions. GLER also captures the seasonal variations and cross-track dependence of the OMI-derived
20 [LERs](#) [LER](#). We attribute a small negative-bias of GLER data relative to OMI [LERs](#) [LER](#) in most regions to remaining effects of non-absorbing aerosol and/or cloud contamination and to small differences in MODIS and OMI calibration. Our evaluation has demonstrated that the GLER concept can reliably and efficiently account for surface BRDF effects within UV-Vis cloud and trace-gas retrieval algorithms. In addition, [GLERs](#) [GLER](#) can be easily incorporated into the existing algo-
25 rithms.

~~Cox-Munk slope distribution over water surfaces and ancillary input data sets To characterize scattering anisotropy over water surfaces, we consider light specularly reflected from a rough water surface as well as diffuse light backscattered by water bulk and transmitted through the water surface. We account for polarization at the ocean surface using a full Fresnel reflection matrix as derived
30 by Mishechenko and Travis (1997). We also consider contributions from oceanic foam that can be significant for high wind speeds. Diffuse light from the ocean is described by a Case 1 water model that has chlorophyll concentration as a single input parameter (Morel, 1988). Our Case 1 water model accounts for the anisotropic nature of light backscattered by the ocean (Morel and Gentili, 1996).~~

~~Details regarding the ancillary data sets used for water GLER calculation are provided in Table ??.~~ Pixel chlorophyll concentration is needed to calculate the water-leaving radiance contribution; wind speed and direction are essential input parameters for sunlint intensity calculation. Here, a 2.5-
monthly climatology of chlorophyll-a concentration derived with Aqua MODIS Ocean Color Chlorophyll (OCI) algorithm (<https://oceancolor.gsfc.nasa.gov/atbd/chlor-a/>) is selected ~~this dataset has excellent cloud screening and calibration as compared with other sensors including Terra MODIS. We use sea-surface wind speed retrieval from the Advanced Microwave Scanning Radiometer for EOS
5 (AMSR-E) on board Aqua, which is followed closely by the Aura platform (with OMI). AMSR-E~~

has high spatial resolution (0.25°) grids (Wentz and Meissner, 2004). 2-D interpolation is applied to obtain the averaged wind speed over an OMI pixel FOV. Since AMSR-E is not available after October 2011, we switch to the first Special Sensor Microwave Imager/Sounder (SSMIS) F16 satellite (launched in Oct, 2003) data (F16 SSMIS). The SSMIS-derived wind speed has the same spatial resolution as AMSR-E (<https://ghre.nsstc.nasa.gov/hydro/details/rssmif16d>). Wind direction is specified from NASA Global Modeling and Assimilation Office (GMAO) Forward Processing for Instrument Teams (FP-IT) data ($0.625^\circ \times 0.5^\circ$ grids at every one hour, see GMAO at https://gmao.gsfc.nasa.gov/GMAO_products/ for more information). For those ancillary data that have coarser spatial but higher temporal resolutions than those of OMI itself, such as the wind direction dataset, a 2-D collocation (time and space) and interpolation is applied to obtain the average over the OMI FOV. Spatial and temporal resolutions of ancillary data used for water GLER calculation

Name	Source	Spatial	Temporal
0.5exChlorophyll-a concentration	MODIS Aqua	$2.5'$	monthly
Wind speed (before Oct 2011)	AMSR-E/Aqua	0.25°	N/A
Wind speed (after Oct 2011)	SSMIS/F16	0.25°	N/A
Wind direction	FP-IT/GMAO	$0.625^\circ \times 0.5^\circ$	1 hour

20 Appendix A Pixel-averaged terrain height and pressure

Appendix A Ancillary data preprocessing

A1 Ancillary data collocation

The collocation methodology is shown schematically in Figure 12. The OMI pixel is first defined from the four ground pixel corner points provided in the OMPICOR data product as a 4-sided polygon. A sample space is then constructed along constant latitudinal boundaries, with the corner points tangent to the boundaries of the sample space as shown. All pixels from the MODIS BRDF/Albedo product and ancillary data sets inside the sample space are tested using the point-in-polygon method (Haines, 1994). For this application, we used the corner points for the VIS channel, corresponding to 75% of the energy in the along-track field of view. This definition assumes the pixels across the track share boundaries with their two adjacent neighbors (except for the pixels at the far edge of the swath), while the pixels along the track of the satellite overlap (reference to OMPICOR Readme). de Graaf et al. (2016) showed the actual shape of the OMI pixel is not exactly a rectangular polygon but rather is best represented by a super Gaussian. They also showed that the optimal overlap function between OMI and MODIS depends on the scene and the time difference between the satellites. We do not consider these factors as critical to this application because the GLER is based on MCD43GF, an 8-day gridded MODIS BRDF product from Terra and Aqua. Small errors in the pixel shape should only have a minimal impact on our results.

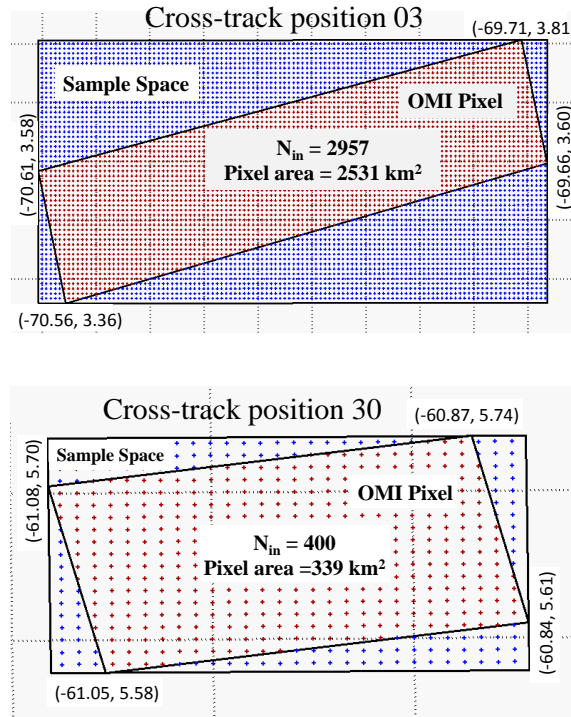


Fig. 12: [An illustration of collocating the high resolution MODIS BRDF data with an OMI pixel FOV. Sample space is defined as the MODIS data space that encloses the entire OMI pixel polygon. \$N_{in}\$ is the number of MODIS data points within the OMI pixel \(red dots\). Numbers at each pixel corner indicate its geolocation \(longitude, latitude\). Two pixels are selected: cross-track position 03 \(near the edge of swath\) and cross-track position 30 \(near nadir\) for orbit 12399 with along-track position 1000.](#)

5 A2 [Pixel averaged terrain height and pressure](#)

In order to estimate the pixel-based surface pressure, a critical input parameter to the air mass factor in the NO_2 algorithm as well as to total optical depth of the Rayleigh atmosphere, terrain height derived from high resolution DEM data averaged over OMI pixel FOV is required. In the GLER product, we derived pixel average terrain height from surface topographic data (ETOPO2v2), 2' gridded global relief data with the vertical precision of 1 m from the NOAA National Centers for Environmental Information (NCEI) Marine Geology and Geophysics (<https://www.ngdc.noaa.gov/mgg/global/etopo2.html>), in which positive values represent altitude above sea level while negative values represent depth below sea level. To derive the correct terrain height, we need first to determine the surface type for each ETOPO2v2 cell. This can be done by preprocessing the ETOPO2v2 data with the 30" MODIS land-water flag map described in Section [2.22.3](#). If the cell's surface type is land or inland water, we keep both positive and negative values; if it is ocean, we zero out negative values.

Then we average the preprocessed ETOPO2v2 data within the OMI FOV. This approach produces a less noisy result for terrain height than the original OMI L1b terrain height which is the value at the center of the pixel (see Figure 13).

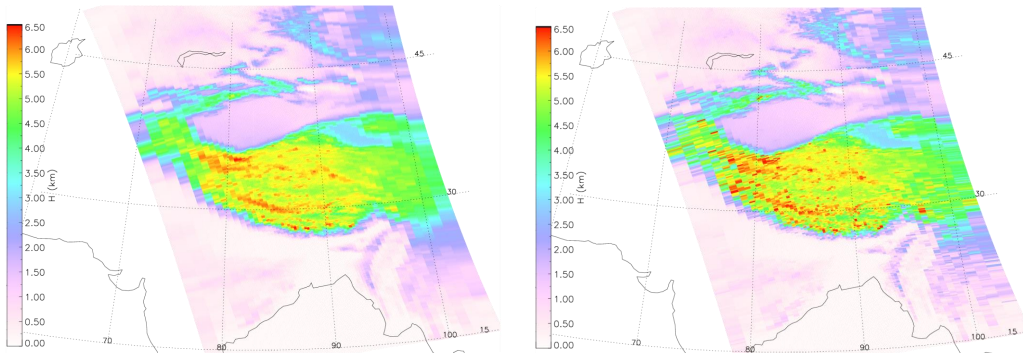


Fig. 13: Pixel average terrain height for region of the Tibetan plateau from ETOPO2v2 used in GLER (left), and OMI L1b terrain height at the center of the pixel (right).

Given the pixel average terrain height (z), the terrain pressure (P_s) for the OMI pixel is calculated
 10 as

$$P_s = P_s(\text{GMI}) \exp\left(-\frac{z - z(\text{GMI})}{H}\right), \quad (\text{A1})$$

$$H = (kT)/(Mg) \quad (\text{A2})$$

where $P_s(\text{GMI})$ is the surface pressure monthly climatology (1° latitude by 1.25° longitude spatial resolution) taken from the Global Modeling Initiative (GMI) chemistry transport model driven
 15 by fields from the NASA GMAO Goddard Earth Observing System 5 (GEOS-5) global data assimilation system (Rienecker et al., 2011), $z(\text{GMI})$ is the terrain height at the GMI resolution of $1^\circ \times 1.25^\circ$, k is Boltzmann constant, T is the GMI air temperature at the surface, M is the mean molecular weight of air, and g is the acceleration due to gravity.

Appendix B Look-up tables

20 From an operational point of view, it is impractical to process OMI and similar satellite data with on-line radiative transfer calculations. For example, for OMI there are more than 14 years of global data, and there will be a much larger data turn-round for the recently launched TROPOspheric Monitoring Instrument ([TropOMI](#)[TROPOMI](#)) and the upcoming TEMPO mission (Tropospheric Emissions: Monitoring of Pollution). Since our goal is to create a global GLER product for generic satellite missions, a look-up-table (LUT) approach is adopted to calculate variables in Eq. 2 such as I_{comp} , I_0 , T

5 and S_b at different surface pressure levels (see Table 4 for details). These LUTs have sufficient nodes
to cover all possible OMI geometries (SZA, VZA and RAA) and model input parameters, such as
three surface BRDF kernel coefficients (f_{iso} , f_{vol} , and f_{geo}) for land and chlorophyll concentration,
wind speed and direction for waters ~~at different surface pressure levels.~~ The LUT approach has
been validated with online VLIDORT calculations; this shows a satisfactory results of better than
10 0.5% relative differences between online calculations and interpolated TOA radiances.

Table 4: LUT structures for input parameters

Parameter	Number of nodes	Step(s)	Range
Pressure	11	20-110	411-1100 hPa
SZA	45	2	0-86°
VZA	41	2	0-80°
RAA	48	2-5	0-180°
f_{iso}	25	0.01-0.04	0.01-0.999
f_{vol}	16	0.01-0.1	0-0.5
f_{geo}	12	0.005-0.02	0-0.1
Chlorophyll	24	0.003-3.0	0.01-10 mg/m ³
Wind speed	23	0.2-5.0	0.001-50 m/s
Wind direction	36	10	0-360°

~~Author contributions: WQ wrote the manuscript, developed the GLER algorithm and created the
GLER product. ZF computed~~

Appendix C Cloud Screen Selection

An important consideration for the method of evaluating the GLER data is properly removing cloudy
15 scenes from the analysis. For this work, the O₂-O₂ product ECF was used for the removal of cloudy
OMI scenes because this ECF will be used in NO₂ retrievals that the GLER product aims to improve.
Since the O₂-O₂ ECF depends on the GLER and OMI TOA Radiances, care was taken into analyzing
the distribution of the GLER and OMI-derived LER difference for various cloud fraction cutoffs.
20 Figure 14 shows the distribution of the difference between GLER and OMI-derived LER across
various geographical regions for five different possible ECF cutoffs. The mode of the distribution
likely represents the majority of cloud free scenes and can be thought of as a representation of the
bias between the calculated GLER and measured OMI-derived LER. We note that on the right side
of the distribution there is a small tail where OMI-derived LER is less than GLER. This could be
caused either by the uncertainty of the MODIS measurements or absorbing aerosols that are not
25 being completely removed with the AI screen. To capture both the mode of the distribution as well
as possible noise in the measurements which could be within the right tail of the distribution, the

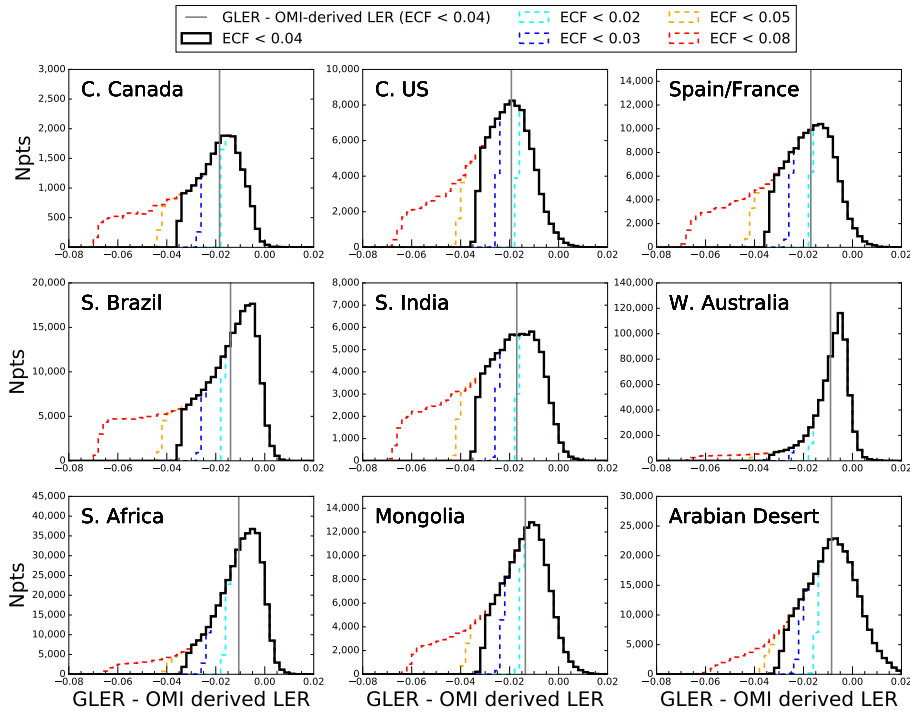


Fig. 14: Histograms showing the distribution of the difference between GLER and OMI-derived LER for various O_2-O_2 ECF screens across different geographical regions in 2006. While no cloud screening was performed, aerosols were removed and OMI scenes with land fraction $< 99\%$ were not included. The vertical grey line represents the mean of the difference between GLER and OMI-derived LER for the various regions. The dark black line representing ECF < 0.04 was the cloud screen implemented in the evaluation of GLER for this paper.

ECF cutoff of 4% is used for the evaluation. We note that this cutoff may leave some residual clouds in regions such as western Australia where the left tail is larger than the right tail, but have decided to use a consistent cloud screen for all regions and note that the extra number of possible cloud contaminated data in the left tail are much less than the number of data within the mode of the distribution.

While these histograms suggest that the mode of the GLER - OMI-derived LER difference is likely most representative of the cloud free OMI scenes, in this work we present the mean of the difference. In the evaluation we examine regions such as that include month with extreme cloudiness or constant snow cover. For these months, since the number of available data are limited for evaluation, the distribution of the data becomes quite flat making the mode difficult to determine. As shown in Figure 14 the mean of the difference is nearly identical to the mode in regions such as the Arabian Desert and Central United States, while in other regions such as southern Brazil and southern Africa the mean of the difference is lower than the mode difference by nearly 0.01. This possibly suggests

5 that the mean of the difference is more influenced by the residual cloud and aerosol than the mode
of the difference. For this reason, it is possible that the bias between the calculated and measured
LER is slightly smaller than the mean difference presented in this work.

Appendix D Relative calibration of OMI and MODIS

10 Jaross and Warner (2008) compared 2004–2005 radiances from OMI and MODIS to TOA radiance
predicted using a radiative transfer model over Antarctica. We use these results to indirectly compare
the calibration of OMI and MODIS radiances. Figure 9a of Jaross and Warner, reproduced here as
Figure 15, shows that MODIS band 3 reflectances near 470 nm in Collection 4 data were around 1%
high relative to the model at nadir, and OMI Collection 2 L1B data were approximately 2.5% lower
than the model for similar viewing conditions. Based on this result, the OMI calibration team applied
15 a +2.5% time-independent, wavelength-independent calibration adjustment to OMI Collection 3
radiances to bring the L1B into agreement with the model (Dobber et al., 2008; Jaross and Warner, 2008).
The MODIS radiance calibration was unchanged between Collections 4 and analyzed the comparison
results 5 for the period Jaross and Warner examined, therefore the MODIS Collection 5 radiances
are higher than OMI Collection 3 radiances by approximately 1%. This is within the 2% uncertainty
estimated for the model. The agreement is also within the theoretical combined uncertainty calculated

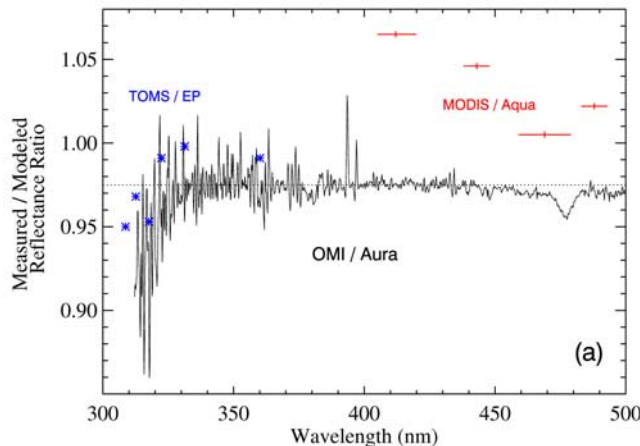


Fig. 15: The mean ratios of TOA satellite reflectances to a model used over Antarctica for validation
during the 2004 solstice; OMI (solid line), MODIS (red bars), and TOMS/Earth Probe (asterisks).
Data shown are for the interval $62^\circ \leq \theta_0 \leq 68^\circ$ ($47^\circ \leq \theta_0 \leq 52^\circ$ for TOMS/Earth Probe).
Uncertainties on MODIS bands other than band 3 (470 nm) are estimated to be several percent.
Reproduced from figure 9a of (Jaross and Warner, 2008).

20 from the uncertainties reported for each instrument independently in the literature. The error in
OMI radiometric calibration at nadir is 2%, uncertainty in swath dependence is also within 2%

(Dobber et al., 2008), so we estimate the combined calibration uncertainty of OMI is 2-3%. The MODIS total uncertainty is 2% (Xiong et al., 2005), therefore the theoretical combined uncertainty in the difference between OMI and MODIS is 3-4%. In order to explain the bias in GLER - OMI LER of 0.01 to 0.02, the MODIS radiances would have to be biased 3-6% low relative to OMI, so it is unlikely that calibration difference is the main cause of the bias in our GLER comparisons. The bias is most likely due to a combination of the relative calibration differences and the presence of residual cloud and aerosol contamination that increase the measured OMI radiances relative to those we simulate with GLER. ~~DH supported the GLER development and contributed writing Sect 2.2 and Sect 4. AV proposed the GLER concept and supported implementation of the algorithm. JJ supported the GLER development and provided a general framework of the manuscript. NK proposed the GLER concept and supported the GLER development. BF provided coding support~~

Time dependent degradation of the instruments is also a factor to consider when comparing the relative instrument calibration. Jaross and Warner performed their analysis with the first few years of overlap in the OMI and MODIS data and did not examine long-term instrument drift. Schenkeveld et al. (2017) estimated that the long-term degradation of OMI reflectances at 466 nm is 1-1.5% from 2004 to present. This drift has not been corrected in the Collection 3 L1B radiance or the GLER products. The MODIS Aqua solar reflective bands including band 3 were corrected for time-dependent drift in Collection 5 (Wu et al., 2013), but errors in MODIS Terra due to anomalous degradation of up to 5% across the scan appeared around 2007, and this error was not sufficiently corrected in Collection 5 (Lyapustin et al., 2014). We see no evidence of the impact of such a drift on the GLER product or the BRDF itself, so we suspect that poor quality MODIS Terra data were excluded when the MCD43GF product was generated.

Data availability. GLER will be available at https://aura.gesdisc.eosdis.nasa.gov/data/Aura_OMI_Level2/. The MODIS gap-filled BRDF Collection 5 product MCD43GF used for calculation of GLER in this paper is available at <ftp://rsftp.eos.umb.edu/data02/Gapfilled/> (last access: 11 March 2019). The OMI Level 1 data used for calculations of GLER are available at https://aura.gesdisc.eosdis.nasa.gov/data/Aura_OMI_Level1/ (last access: 11 April 2019). The OMI Level 2 Collection 3 data that include NO₂ and OMI pixel corner products are available at https://aura.gesdisc.eosdis.nasa.gov/data/Aura_OMI_Level2/ (last access: 11 April 2019). OMI O₂-O₂ Cloud product can be provided upon request of the co-authors.

Author contributions. WQ led the paper and was the primary developer of the GLER algorithm. WQ, ZF, and DH wrote the paper. ZF and WQ performed the GLER analysis. ZF and DH designed the GLER analysis. AV and NK contributed to the GLER analysis and preparation of the paper. JJ provided guidance throughout the development of the manuscript. BF contributed tools and expertise for MODIS-OMI pixel collocation. RS developed the VLIDORT code ~~needed for computation of radiance LUTs~~ used for the BRDF and radiance computations.

Competing interests. The authors declare that they have no conflict of interest.

Acknowledgements. Funding for this work was provided by NASA through Aura core team funding as well as the Aura project and Aura Science Team and Atmospheric Composition Modeling and Analysis Program managed by Kenneth Jucks and Barry Lefer. We acknowledge Crystal Schaaf for providing gap-filled MODIS MCD43GF BRDF data, ~~and~~ the MODIS data processing team, as well as the OMI calibration ~~team and data processing teams~~ at KNMI and NASA. We ~~thank Alexei Lyapustin and Crystal Schaaf for helpful discussions.~~ gratefully acknowledge helpful discussions with Alexei Lyapustin, Crystal Schaaf, Glen Jaross, members of the MODIS Characterization Support Team, and Sriharsha Madhavan.

20 References

- Boersma, K. F., Eskes, H. J., Dirksen, R. J., van der A, R. J., Veefkind, J. P., Stammes, P., Huijnen, V., Kleipool, Q. L., Sneep, M., Claas, J., Leitão J., Richter, A., Zhou, Y., and Brunner, D.: An improved tropospheric NO₂ column retrieval algorithm for the Ozone Monitoring Instrument, *Atmos. Meas. Tech.*, 4, 1905–1928, doi:10.5194/amt-4-1905-2011, 2011.
- 25 Bodhaine, B. A., Wood, N. B., Dutton, E. G., and Slusser, J. R.: On Rayleigh Optical Depth Calculations, *J. Atmos. Ocean. Tech.*, 16: 1854–1861, doi:10.1175/1520-0426,1999.
- [Cescatti, A., Marcolla, B., Vannan, S. K. S., Pan, J. Y., Romn, M. O., Yang, X., Ciais, P., Cook, R. B., Law, B. E., Matteucci, G., Migliavacca, M., Moors, E., Richardson, A. D., Seufert, G., and Schaaf, C. B.: Intercomparison of MODIS albedo retrievals and in situ measurements across the global FLUXNET network, *Remote Sens. Environ.*, 121, 323–334, 2012.](#)
- 30 [Coddington, O., Schmidt, K. S., Pilewskie, P., Gore, W. J., Bergstrom, R. W., Romn, M., Redemann, J., Russell, P. B., Liu, J., and Schaaf, C. B.: Aircraft measurements of spectral surface albedo and its consistency with ground-based and space-borne observations, *J. Geophys. Res.*, 113, doi:10.1029/2008JD010089, 2008.](#)
- Cox, C. and Munk, W.: Statistics of the sea surface derived from sun glitter, *J. Mar. Res.* 13, 198–227, 1954.
- 35 Dave, J. V.: Effect of aerosol on the estimation of total ozone in an atmospheric column from the measurements of the ultraviolet radiance, *J. Atmos. Sci.*, 35, 899–911, 1978.
- [de Graaf, M., Sihler, H., Tilstra, L. G., and Stammes, P.: How big is an OMI pixel? *Atmos. Meas. Tech.*, 9, 3607–3618, doi:10.5194/amt-9-3607-2016, 2016.](#)
- Dobber, M., Q. Kleipool, R. Dirksen, P. Levelt, G. Jaross, S. Taylor, T. Kelly, L. Flynn, G. Leppelmeier, and
- 40 Rozemeijer, N.: Validation of Ozone Monitoring Instrument level 1b data products, *J. Geophys. Res.*, 113, D15S06, doi:10.1029/2007JD008665, 2008.
- Fisher, B., Joiner, J., Vasilkov, A., Veefkind, P., Platnick, S., and Wind, G.: A New A-train Cloud Product that Co-locates OMI and MODIS Cloud and Radiance Parameters onto the OMI Footprint. EOS Aura Science Team Meeting, College Park, MD United States, 2014. Available at
- 5 <https://ntrs.nasa.gov/search.jsp/?R=20150001342>.
- Franch, B., Vermote, E. F., Sobrino, J. A., and Fedele, E.: Analysis of directional effects on atmospheric correction, *Remote Sens. Environ.*, 128, 276–288, 2013.
- [Gao, B. C., and Kaufman, Y. J.: Water vapor retrievals using Moderate Resolution Imaging Spectroradiometer \(MODIS\) near-infrared channels, *J. Geophys. Res.*, 108, 4389, doi:10.1029/2002JD003023, 2003](#)
- 10 Haines, E. : Point in Polygon Strategies, *Graphics Gems IV*, ed. Paul Heckbert, Academic Press, pp. 24–46, 1994.
- Herman, J. R. and Celarier, E.: Earth surface reflectivity climatology at 340 to 380 nm from TOMS data, *J. Geophys. Res.*, 102, 28003–28011, 1997.
- [Holben, B.N., Eck, T.F., Slutsker, I., Tanr, D., Buis, J.P., Setzer, A., Vermote, E.F., Reagan, J.A., Kaufman, Y.J., Nakajima, T., Lavenue, F., Jankowiak, I., and Smirnov, A.: AERONET - A federated instrument network and data archive for aerosol characterization, *Remote Sens. Environ.*, 66, 1-16, 1998.](#)
- 15 Jaross, G., and J. Warner, J.: Use of Antarctica for validating reflected solar radiation measured by satellite sensors, *J. Geophys. Res.*, 113, D16S34, doi:10.1029/2007JD008835, 2008.
- [Jin, Y., Schaaf, C. B., Woodcock, C. E., Gao, F., Li, X., Strahler, A. H., Lucht, W., and Liang, S.:](#)

- 20 [Consistency of MODIS surface BRDF/Albedo retrievals: 2. Validation, J. Geophys. Res., 108, 4159, doi:10.1029/2002JD002804, 2003.](#)
- Justice, C. O., Vermote, E., Townshend, J. R. G., Defries, R., Roy, D. P., Hall, D. K., Salomonson, V. V., Privette, J. L., Riggs, G., Strahler, A., Lucht, W., Myneni, R. B., Lewis, P., and Barnsley, M. J.: The Moderate Resolution Imaging Spectroradiometer (MODIS): Land remote sensing for global change research, IEEE Trans. Geosci. Remote Sens., 36, 1228-1249, 1998.
- 25 Kay, S. J. D., Hedley, and Lavender, S.: Sun glint correction of high and low spatial resolution images of aquatic scenes: a review of methods for visible and near-Infrared wavelengths, Remote Sensing, 1, 697–730, doi:10.3390/rs1040697, 2009.
- Kleipool, Q. L., Dobber, M. R., de Haan, J. F., and Levelt, P. F.: Earth surface reflectance climatology from 30 years of OMI data, J. Geophys. Res., 113, D18308, doi:10.1029/2008jd010290, 2008.
- Knobelspiesse, K. D., Cairns, B., Schmid, B., Roman, M. O., and Schaaf, C. B.: Surface BRDF estimation from an aircraft compared to MODIS and ground estimates at the Southern Great Plains site, J. Geophys. Res., 113, D20105, doi:10.1029/2008JD010062, 2008.
- Koelemeijer, R. B. A., Stammes, P., Hovenier, J. W., and de Haan, J. F.: A fast method for retrieval of cloud 35 parameters using oxygen A-band measurements from the Global Ozone Monitoring Experiment, J. Geophys. Res., 106, 3475–3496, 2001.
- Kotchenova, S. Y., and Vermote, E. F.: Validation of a vector version of the 6S radiative transfer code for atmospheric correction of satellite data. Part II: Homogeneous Lambertian and anisotropic surfaces, Appl. Opt., 46(20), 4455–4464, doi:10.1364/AO.46.004455, 2007.
- 40 Krotkov, N. A., Lamsal, L. N., Celarier, E. A., Swartz, W. H., Marchenko, S. V., Bucsela, E. J., Chan, K. L., Wenig, M., and Zara, M.: The version 3 OMI NO₂ standard product, Atmos. Meas. Tech., 10, 3133-3149, <https://doi.org/10.5194/amt-10-3133-2017>, 2017.
- Lamsal, L. N., Krotkov, N. A., Celarier, E. A., Swartz, W. H., Pickering, K. E., Bucsela, E. J., Gleason, J. F., Martin, R. V., Philip, S., Irie, H., Cede, A., Herman, J., Weinheimer, A., Szykman, J. J., and Knepp, 5 T. N.: Evaluation of OMI operational standard NO₂ column retrievals using in situ and surface-based NO₂ observations, Atmos. Chem. Phys., 14, 11587-11609, doi:10.5194/acp-14-11587-2014, 2014.
- Li, X., Strahler, A.H.: Geometric-optical bidirectional reflectance modeling of the discrete crown vegetation canopy: effect of crown shape and mutual shadowing, IEEE Trans. Geosci. Remote Sens., 30, 276–292, 1992.
- Liu, J., Schaaf, C., Strahler, A., Jiao, Z., Shuai, Y., Zhang, Q., Roman, M., Augustine, J. A., and Dutton, 10 E. G.: Validation of Moderate Resolution Imaging Spectroradiometer (MODIS) albedo retrieval algorithm: Dependence of albedo on solar zenith angle, J. Geophys. Res., 114, D01106, doi:10.1029/2008JD009969, 2009.
- Lorente, A., Boersma K. F., Stammes, P., Tilstra, L. G., Richter, A., Yu, H., Kharbouche, S., and Muller, Jan-Peter: The importance of surface reflectance anisotropy for cloud and NO₂ retrievals from GOME-2 and 15 OMI, Atmos. Meas. Tech., 11, 4509-4529, <https://doi.org/10.5194/amt-11-4509-2018>, 2018.
- Lucht, W., Schaaf, C. B., and Strahler, A. H.: An algorithm for the retrieval of albedo from space using semiempirical BRDF models, IEEE T. Geosci. Remote Sens., 38, 977–998, 2000.
- Lyapustin, A., Wang, Y., Laszlo, I., Hilker, T., Hall, F., Sellers, P., Tucker, J., Korkin, S.: Multi-angle implementation of atmospheric correction for MODIS (MAIAC). 3: Atmospheric correction, Rem. Sens. Environ.,

- 20 <http://dx.doi.org/10.1016/j.rse.2012.09.002>, 2012.
- [Lyapustin, A., Wang, Y., Xiong, X., Meister, G., Platnick, S., Levy, R., Franz, B., Korkin, S., Hilker, T., Tucker, J., Hall, F., Sellers, P., Wu, A., and Angal, A.: Scientific impact of MODIS C5 calibration degradation and C6+ improvements, *Atmos. Meas. Tech.*, 7, 4353–4365, <https://doi.org/10.5194/amt-7-4353-2014>, 2014.](#)
- 25 Martonchik, J. V., Bruegge, C. J., and Strahler, A. H.: A review of reflectance nomenclature used in remote sensing, *Remote Sens. Reviews*, 19, 9–20, 2000.
- McLinden, C. A., Fioletov, V., Boersma, K. F., Kharol, S. K., Krotkov, N., Lamsal, L., Makar, P. A., Martin, R. V., Veefkind, J. P., and Yang, K.: Improved satellite retrievals of NO₂ and SO₂ over the Canadian oil sands and comparisons with surface measurements, *Atmos. Chem. Phys.*, 14, 3637–3656, doi:10.5194/acp-14-3637-2014, 2014.
- 30 Mishchenko, M. I. and Travis, L. D.: Satellite retrieval of aerosol properties over the ocean using polarization as well as intensity of reflected sunlight, *J. Geophys. Res.*, 102, 16989–17013, doi:10.1029/96JD02425, 1997.
- Morel, A.: Optical modeling of the upper ocean in relation to its biogeochemical matter content (Case I waters), *J. Geophys. Res.*, 93, 10749–10768, 1988.
- Morel, A. and Gentili, B.: Bidirectional reflectance of oceanic water. III. Implication of bidirectionality for the remote-sensing probe, *Appl. Opt.*, 35, 4850–4862, 1996.
- 35 Nolin, A., Armstrong, R., and Maslanik, J.: Near real-time SSM/I EASE-grid daily global ice concentration and snow extent, Digit. Media, Natl. Snow Ice Data Center, Boulder, CO, USA, 2005.
- Noguchi, K., Richter, A., Rozanov, V., Rozanov, A., Burrows, J. P., Irie, H., and Kita, K.: Effect of surface BRDF of various land cover types on geostationary observations of tropospheric NO₂, *Atmos. Meas. Tech.*, 7, 3497–3508, doi:10.5194/amt-7-3497-2014, 2014.
- 40 Nicodemus, F.: Directional reflectance and emissivity of an opaque surface, *Appl. Opt.*, 4, 767–775, 1965.
- Nicodemus, F. E., et al. (1977). Geometrical considerations and nomenclature for reflectance. Washington, DC: National Bureau of Standards, US Department of Commerce. URL: <http://physics.nist.gov/Divisions/Div844/facilities/specphoto/pdf/geoConsid.pdf>
- 5 Qin, W., Goel, N. S., and Wang, B.: The hotspot effect in heterogeneous vegetation canopies and performances of various hotspot models, *Remote Sens. Reviews*, 14, 283–332, 1996.
- Rienecker, M. M., Suarez, M. J., Gelaro, R., Todling, R., Bacmeister, J., Liu, E., Bosilovich, M. G., Schubert, S. D., Takacs, L., Kim, G.-K., Bloom, S., Chen, J., Collins, D., Conaty, A., da Silva, A., Gu, W., Joiner, J., Koster, R. D., Lucchesi, R., Molod, A., Owens, T., Pawson, S., Pegion, P., Redder, C. R., Reichle, R., Robertson, F. R., Ruddick, A. G., Sienkiewicz, M., and Woollen, J.: MERRA: NASA's Modern-Era Retrospective Analysis for Research and Applications, *J. Climate*, 24, 3624–3648, doi:10.1175/JCLI-D-11-00015.1, 2011.
- 10 [Remer, L.A., Kaufman, Y.J., Tanr, D., Mattoo, S., Chu, D.A., Martins, J.V., Li, R-R., Ichoku, C, Levy, R. C., Kleidman, R.G., Eck, T.F., Vermote, E., and Holben, B.N.: The MODIS Aerosol Algorithm, Products and Validation, *J. Atmos. Sci.*, 62, 947–973, 2005.](#)
- Renz, A. N., and R. A. Ryerson (Editors), 1999, Manual of Remote Sensing, Volume 3, Remote Sensing for the Earth Sciences, 3rd Edition BOOK, ISBN: 978-0-471-29405-4, Wiley, 1999.
- Riggs, G.A., D.K. Hall, and M.O. Romn, 2016. MODIS Snow Products Collection 6 User Guide, NASA MODIS project document.

- 20 Roman, M. O., Schaaf, C. B., Woodcock, C. E., Strahler, A. H., Yang, X., Braswell, R. H., Curtis, P. S., Davis, K. J., Dragoni, D., Goulden, M. L., Gu, L., Hollinger, D. Y., Kolb, T. E., Meyers, T. P., Munger, J. W., Privette, J. L., Richardson, A. D., Wilson, T. B., and Wofsy, S. C.: The MODIS (Collection V005) BRDF/albedo product: Assessment of spatial representativeness over forested landscapes, *Remote Sens. Environ.*, 113, 2476-2498, 2009.
- 25 Roman, M. O., Gatebe, C. K., Shuai, Y., Wang, Z., Gao, F., Masek, J. G., He, T., Liang, S., and Schaaf, C. B.: Use of in situ and airborne multiangle data to assess MODIS- and Landsat-based estimates of directional ~~reflectance~~[reflectance](#) and albedo, *IEEE Trans. Geosci. Remote Sens.*, 51, 1393-1403, 2013.
- Roujean, J., Leroy, M., Deschamps, P. A bidirectional reflectance model of the Earth's surface for the correction of remote sensing data, *J. Geophys. Res.*, 97, 20455–20468, 1992.
- 30 Ross, J. V, *The Radiation Regime and Architecture of Plant Stands 3. BOOK*, Springer Science & Business Media, 1981.
- Salomon, J. G., Schaaf, C. B., Strahler, A. H., Gao, F., and Jin Y.: Validation of the MODIS bidirectional reflectance distribution function and albedo retrievals using combined observations from the Aqua and Terra platforms, *IEEE Trans. Geosci. Remote Sens.*, 44, 1555-1565, 2006.
- 35 Schaaf, C. B., Gao, F., Strahler, A. H., Lucht, W., Li, X., Tsang, T., Strugnell, N. C., Zhang, X., Jin, Y., Muller, J.-P., Lewis, P., Barnsley, M., Hobson, P., Disney, M., Roberts, G., Dunderdale, M., Doll, C., d'Entremont, R., Hu, B., Liang, S., and Privette, J. L.: First operational BRDF, albedo and nadir reflectance products from MODIS, *Remote Sens. Environ.*, 83, 135–148, 2002.
- Schaaf, C. L. B., Liu, J., Gao, F., and Strahler, A. H.: MODIS albedo and reflectance anisotropy products from Aqua and Terra, In *Land Remote Sensing and Global Environmental Change: NASA's Earth Observing System and the Science of ASTER and MODIS, Remote Sensing and Digital Image Processing Series, Vol.11*, B. Ramachandran, C. Justice, M. Abrams, Eds, Springer-Verlag, 873 pp., 2011.
- Schaepman-Strub, G., Schaepman, M. E., Painter, T. H., Dangel, S., Martonchik, J. V., Reflectance quantities in optical remote sensing—definitions and case studies, *Remote Sens. Environ.*, 103, 27–42, 2006.
- 5 Schenkeveld, V. M. E., Jaross, G., Marchenko, S., Haffner, D., Kleipool, Q. L., Rozemeijer, N. C., Veeffkind, J. P., and Levelt, P. F.: In-flight performance of the Ozone Monitoring Instrument, *Atmos. Meas. Tech.*, 10, 1957–1986, doi:10.5194/amt-10-1957-2017, 2017.
- Sobrino, J.A., Franch, B., ~~Oltra-Carri~~[Oltra-Carri](#), R., Vermote, E. F., and Fedele, E.: Evaluation of the MODIS Albedo product over a heterogeneous agricultural area, *Int. J. Remote Sensing*, 34, 5530–5540, 2013.
- 10 Spurr, R. J. D.: VLIDORT: a linearized pseudo-spherical vector discrete ordinate radiative transfer code for forward model and retrieval studies in multilayer multiple scattering media, *J. Quant. Spectr. Rad. Trans.*, 102, 316–421, 2006.
- [Sun, J., Xiong, X., Angal, A., Chen, H., Wu, A. X., and Geng, X.: Time-Dependent Response Versus Scan Angle for MODIS Reflective Solar Bands, IEEE Trans. Geosci. Remote Sens., 52, 3159–3174, 2014.](#)
- 15 Sun, Q., Wang, Z., Li, Z., Erb, A., and Schaaf, C. B.: Evaluation of the global MODIS 30 arc-second spatially and temporally complete snow-free land surface albedo and reflectance anisotropy dataset, *Intl. J. Appl. Earth Obs. Geoinfo.*, 58, 36–49, doi:10.1016/j.jag-01-011-2017, 2017.
- [Susaki, J., Yasuoka, Y., Kajiwara, K., Honda, Y., and Hara, K.: Validation of MODIS albedo products of paddy fields in Japan, IEEE Trans. Geosci. Remote Sens., 45, 206–217, 2007.](#)

- 20 [Tilstra, L. G., Tuinder, O. N. E., Wang, P., and Stammes, P.: Surface reflectivity climatologies from UV to NIR determined from Earth observations by GOME-2 and SCIAMACHY, *J. Geophys. Res.*, 122, <https://doi.org/10.1002/2016JD025940>, 2017.](#)
- Torres, O., Tanskanen, A., Veihelman, B., Ahn, C., Braak, R., Bhartia, P. K., Veefkind, V., and Levelt, P.: Aerosols and Surface UV Products from OMI Observations: An Overview, *J. Geophys. Res.*, 112, D24S47, doi:10.1029/2007JD008809, 2007.
- 25 Vasilkov, A. P., Qin, W., Krotkov, N., Lamsal, L., Spurr, R., Haffner, D., Joiner, J., Yang, E.-S., and Marchenko, S., Accounting for the effects of surface BRDF on satellite cloud and trace-gas retrievals: a new approach based on geometry-dependent Lambertian equivalent reflectivity applied to OMI algorithms, *Atmos. Meas. Tech.*, 10, 333–349, doi:10.5194/amt-10-333-2017, 2017.
- 30 Vasilkov, A. P., Yang, E.-S., Marchenko, S., Qin, W., Lamsal, L., Joiner, J., Krotkov, N., Bhartia, P. K. and Spurr, R.: A cloud algorithm based on the O₂-O₂ 477 nm absorption band featuring an advanced spectral fitting method and the use of surface geometry-dependent Lambertian-equivalent reflectivity, *Atmos. Meas. Tech.*, 11, 4093–4107, doi:10.5194/amt-11-4093-2018, 2018.
- Veefkind, J. P., de Haan, J. F., Sneep, M., and Levelt, P. F.: Improvements to the OMI (O₂-O₂) operational cloud algorithm and comparisons with ground-based ~~radar~~-radar-lidar observations, *Atmos. Meas. Tech.*, 9, 6035–6049, doi:10.5194/amt-9-6035-2016, 2016.
- 35 Vermote, E.F., Tanre, D., Deuze, J. L., Herman, M., Morcrette, J. J.: Second Simulation of the Satellite Signal in the Solar Spectrum: an overview, *IEEE Trans. Geosci. Remote Sens.*, 35, 675-686, 1997.
- Vermote, E. F., El Saleous, N. Z., Justice, C. O.: Atmospheric correction of MODIS data in the visible to middle infrared: first results, *Remote Sens. Env.*, 83, 97–111, 2002.
- 40 Vermote, E. F., and Kotchenova, S.: Atmospheric correction for the monitoring of land surfaces, *J. Geophys. Res.*, 113, D23S90, doi:10.1029/2007JD009662, 2008.
- Wang, K., Liang, S., Schaaf, C. L., and Strahler, A. H.: Evaluation of Moderate Resolution Imaging Spectroradiometer land surface visible and shortwave albedo products at FLUXNET sites, *J. Geophys. Res.*, 115, D17107, doi:10.1029/2009JD013101, 2010.
- 5 [Wang, Y., Lyapustin, A., Privette, J. L., Cook, R. B., SanthanaVannan, S.K., Vermote, E. F., Schaaf, C.B.: Assessment of biases in MODIS surface reflectance due to Lambertian approximation, *Remote Sens. Env.*, 114, 2791-2801, 2010.](#)
- [Wang, K., Liu, J., Zhou, X., Sparrow, M., Ma, M., Sun, Z., and Jiang, w.: Validation of the MODIS global land surface albedo product using ground measurements in a semidesert region on the Tibetan Plateau, *J. Geophys. Res.*, 109, doi:10.1029/2003JD004229, 2004.](#)
- 10 [Wang, Y., Lyapustin, A., Privette, J. L., Cook, R. B., SanthanaVannan, S.K., Vermote, E. F., Schaaf, C.B.: Assessment of biases in MODIS surface reflectance due to Lambertian approximation, *Remote Sens. Env.*, 114, 2791-2801, 2010.](#)
- 15 Wang, P., Stammes, P., van der A, R., Pinardi, G., and van Roozendael, M.: FRESCO+: an improved O₂ A-band cloud retrieval algorithm for tropospheric trace gas retrievals, *Atmos. Chem. Phys.*, 8, ~~6565~~-6565-6576, doi:10.5194/acp-8-6565-2008, 2008.
- [Wang, Z., Schaaf, C. B., Chopping, M. J., Strahler, A. H., Wang, J., Romn, M. O., Rocha, A. V., Woodcock, C. E., and Shuai, Y.: Evaluation of Moderate-resolution Imaging Spectroradiometer \(MODIS\) snow albedo](#)

- 20 [product \(MCD43A\) over tundra, Remote Sens. Env., 117, 264–280, 2012.](#)
- [Wang, Z., Schaaf, C.B., Strahler, A.H., Chopping, M.J., Romn, M.O., Shuai, Y., Woodcock, C.E., Hollinger, D.Y., and Fitzjarrald, D.R.: Evaluation of MODIS albedo product \(MCD43A\) over grassland, agriculture and forest surface types during dormant and snow-covered periods, Remote Sens. Env., 140, 60–77, 2014.](#)
- 25 Wang, Z, Schaaf, C. B., Sun, Q., Shuai, Y., and ~~Romn~~Romn, M. O., Capturing rapid land surface dynamics with Collection V006 MODIS BRDF/NBAR/Albedo (MCD43) products, Remote Sens. Env., 207, 50-64, <https://doi.org/10.1016/j.rse.2018.02.001>, 2018.
- 1065 Wentz, F. J., Meissner T.: AMSR-E/Aqua L2B Global Swath Ocean Products Derived from Wentz Algorithm V002 (January 2009, June to August 2010). Updated daily. Boulder, Colorado USA: National Snow and Ice Data Center. Digital media, 2004.
- [Wu, A., Xiong, X., Doelling, D., Morstad, D., Angal, A., and Bhatt, R., Characterization of Terra and Aqua MODIS VIS, NIR, and SWIR Spectral Bands Calibration Stability, IEEE T. Geosci. Remote Sens., 51, 4330–4338, doi:10.1109/TGRS.2012.2226588, 2013.](#)
- 1070 [Xiong, X., Sun, J., Wu, A., Chiang, K., Esposito, J., Barnes, W., Terra and Aqua MODIS calibration algorithms and uncertainty analysis, Sensors, Systems, and Next-Generation satellites IX, Proc. SPIE, 5978, 255, doi: 10.1117/12.627631, 2005.](#)
- 1075 Yang, E.-S., Vasilkov, A., Joiner, J., Marchenko, S., Krotkov, N., Haffner, D., and Bhar-
tia, P. K.: A new cloud pressure algorithm based on the (O₂-O₂) absorption band at 477 nm, OMI Science Team Meeting, de Bilt, Netherlands, 2015. Available at http://projects.knmi.nl/omi/research/project/meetings/ostm19/pres_ostm19_20150831.php.
- Zhou, Y., Brunner, D., Spurr, R. J. D., Boersma, K. F., Sneep, M., Popp, C., and Buchmann, B.: Accounting for surface reflectance anisotropy in satellite retrievals of tropospheric NO₂, Atmos. Meas. Tech., 3, 1185–1203, doi:10.5194/amt-3-1185-2010, 2010.
- 1080 [Zhu, Z., and Woodcock, C.: Object-based cloud and cloud shadow detection in Landsat imagery, Remote Sensing of Environment, 118, 83-94, doi:10.1016/j.rse.2011.10.028, 2012.](#)